

# On Model, Algorithms, and Experiment for Micro-Doppler-Based Recognition of Ballistic Targets

**ADRIANO ROSARIO PERSICO**, Student Member, IEEE  
**CARMINE CLEMENTE**, Member, IEEE  
**DOMENICO GAGLIONE**, Student Member, IEEE  
**CHRISTOS V. ILIOUDIS**, Student Member, IEEE  
**JIANLIN CAO**, Student Member, IEEE  
University of Strathclyde, Glasgow, U.K.

**LUCA PALLOTTA**, Member, IEEE  
University of Naples Federico II, Naples, Italy

**ANTONIO DE MAIO**, Fellow, IEEE  
Università degli Studi di Napoli "Federico II", Napoli, Italy

**IAN PROUDLER**  
Loughborough University, Leicestershire, U.K.

**JOHN J. SORAGHAN**, Senior Member, IEEE  
University of Strathclyde, Glasgow, U.K.

**The ability to discriminate between ballistic missile warheads and confusing objects is an important topic from different points of view. In particular, the high cost of the interceptors with respect to tactical missiles may lead to an ammunition problem. Moreover, since the time interval in which the defense system can intercept the missile is very short with respect to target velocities, it is fundamental to**

Manuscript received September 3, 2015; revised February 1, 2016 and July 4, 2016; released for publication August 30, 2016. Date of publication February 7, 2017; date of current version June 7, 2017.

DOI. No. 10.1109/TAES.2017.2665258

Refereeing of this contribution was handled by R. Adve.

This work was supported by the Engineering and Physical Sciences Research Council under Grant EP/K014307/1.

Authors' addresses: A. R. Persico, C. Clemente, D. Gaglione, C. V. Ilioudis, J. Cao, and J. J. Soraghan are with the Centre for Excellence in Signal and Image Processing, University of Strathclyde, Glasgow, G1 1XW, U.K., (E-mail: adriano.persico@strath.ac.uk; carmine.clemente@strath.ac.uk; c.ilioudis@strath.ac.uk; domenico.gaglione@strath.ac.uk; jianlin.cao@strath.ac.uk; j.soraghan@strath.ac.uk); L. Pallotta is with the CNIT, University of Naples Federico II, Naples, 80138, Italy, (E-mail: luca.pallotta@unina.it); A. De Maio is with the Dipartimento di Ingegneria Elettrica e delle Tecnologie dell'Informazione, Università degli Studi di Napoli "Federico II", Via Claudio 21, I-80125 Napoli, Italy, (E-mail: ademaio@unina.it); I. Proudler is with the School of Electronic, Electrical and Systems Engineering, Loughborough University, Leicestershire LE11 3TU, U.K., (E-mail: i.k.proudler@lboro.ac.uk).

0018-9251/16 © 2017 CCBY

minimize the number of shoots per kill. For this reason, a reliable technique to classify warheads and confusing objects is required. In the efficient warhead classification system presented in this paper, a model and a robust framework is developed, which incorporates different micro-Doppler-based classification techniques. The reliability of the proposed framework is tested on both simulated and real data.

## I. INTRODUCTION

The challenge of ballistic missiles (BM) classification is continuing to grow in importance [1]. In particular, two principal factors increase the interest in developing efficient techniques to recognize missiles. The first is economic, because the interceptor missiles are expensive relative to that of tactical missiles. The second factor is tactical and relates to the possibility that there may be numerous missiles and many more objects present. Hence the defense system will have, in general, a limited number of missiles and consequently it is important to maximize the interception success ratio. Another fundamental aspect is that the period in which the missile can be intercepted by the defense system is limited, then it is necessary to recognize the real threats in a cloud of debris and other objects. The detection and recognition of a BM are challenging due to various reasons during different phases of its flight. Generally, a BM trajectory is divided into three parts [2]: boost phase, which comprises the powered flight portion; midcourse phase, which comprises the free-flight portion that constitutes most of the flight time and during which the missile separates from the rest of missile; and the re-entry phase wherein the warhead re-enters the Earth's atmosphere to approach the target. As well as the warhead, the missile releases also confusing objects in order to make the BM detection more difficult for defense systems. These objects come in many different shapes.

The midcourse phase represents the most useful period to intercept the warheads. In fact since the launch point of the BM will normally be a significant distance from the defense radar system, the boost phase does not offer much opportunity to track accurately and to recognize the missile. Moreover, during this phase the missile separates from several boosters, which would result in significant interference. The re-entry phase is not very useful for BM recognition due to its short duration and hence limited time available to destroy them, at a safe distance (the war head could be armed with a nuclear or chemical bomb). For the above mentioned reasons, significant attention is given to the discrimination between warheads and confusing objects throughout the midcourse phase. Warheads and confusing objects exhibit different micromotions that, if appropriately exploited, may be used to distinguish them [2]. In particular, the missile has precession and nutation movements, while the confusing objects wobble after they are released from the warhead. The precession comprises two different motions: conical movement, which is a rotation of the axis of symmetry of the missile in a conical shape, and spinning, that is the rotation of the warhead around its axis of symmetry, as described in [2] and [3]. Since warheads and confusing objects make different micromotions, the micro-Doppler analysis introduced by Chen *et al.* in [4]

can be used for the purpose of information extraction for target classification, because different behaviors produce different signatures [5].

In the last decade, a large amount of research has been conducted on the possibility to use micro-Doppler information to identify different targets in many fields of interest, e.g., human motion classification [6] and air moving target recognition [7]. Most systems use information extracted from the time-frequency distribution (TFD) of radar echoes. In [6], [8], and [9], the features for human motion classification are empirically estimated from the spectrogram. In [10], a set of features is evaluated by using the singular value decomposition (SVD) on the spectrograms and estimating the standard deviation of the first right singular vector. In [11], Molchanov *et al.* propose a method for the extraction of cepstrum- and bicoherence-based features from TFD for aircraft classification. In [12], the features are estimated as the Fourier series coefficients of the spectrogram envelope, whereas in [13] the mel-frequency cepstral coefficients (MFCC) are employed with the main aim to recognize human falling from other motions, which can be used for healthcare applications. Other features that are not extracted from TFD are presented in [7], where a method that employs empirical mode decomposition (EMD) and CLEAN technique is proposed. Moreover, a Greedy Gaussian mixture model based classification technique for ATR with low resolution ground surveillance radars is presented in [14], where the linear predictive coding (LPC) and cepstrum coefficient feature sets are extracted from the data. A micro-Doppler classification method that uses the strongest parts of the cadence velocity diagram (CVD) [15] for the feature vector construction is described in [16]. The algorithm is tested successfully in the case of the discrimination of human motions. However, it requires high storage capabilities as long as the feature vector is composed by the highest cadence frequencies and sampled velocity profiles corresponding to each of them.

The aim of this paper is to demonstrate the capability and reliability of micro-Doppler information [17] for the discrimination between warheads and confusing objects. The determination of the best classification technique is outside the scope of this paper. Instead, we consider three typical techniques that exhibit different properties. In order to understand the micro-Doppler shifts, a high frequency based signal model for the targets of interest is proposed that incorporates the effects of occlusion for all the scattering points. A framework is presented for radar micro-Doppler classification based on the processing of the CVD with different information extraction techniques. In particular, three different techniques for feature extraction from the CVD are presented. The first approach is based on the statistical characteristics of the unit area function obtained by averaging and normalizing the CVD (ACVD). The second method is based on the use of pseudo-Zernike (pZ) moments [5], [18]–[20], and the third one is based on the use of the Gabor filter [21]. The ACVD approach is known to require less computation compared to the other two methods, since a smaller feature vector dimension is used.

The pZ moments are widely used in image processing for pattern recognition due to their useful properties, such as scale, translation, and rotation invariance. In [5], a micro-Doppler-based framework using pZ moments has been presented for classification of human movement. It has been compared with other common classification techniques underlining its better performance. Moreover, the scale invariant property is important for micro-Doppler-based feature due to their more robustness with respect to the angle of view, which affects strictly the maximum frequency shift. Gabor filters have been successfully employed to extract reliable features in several challenges, such as the texture and symbol classification [22], [23] and in the context of face recognition [24], especially due to their scale, translation, rotation, and illumination invariant properties. The last two types of features are selected for their high accuracy of performance. Moreover, since a work on successful employment of Gabor filter for ballistic target classification has been presented in [21], the methods is taken as term of comparison extending the previous work with the application on simulated data and Booster data.

The remainder of the paper is organized as follows. Section II introduces the model for the signal received from BM warheads and confusing object. Section III describes the different feature extraction algorithms. In Section IV, both the simulated and the real dataset used to test the proposed algorithms are described. In Section VI, the effectiveness of the proposed approach is demonstrated showing the classification results on both simulated and real data. Section VI concludes the paper.

## II. SIGNAL MODEL

In this section, the model for the signal scattered from a ballistic target is described. The exact calculation of the received radar signal from a target is usually very difficult because of the scattering mechanisms, even if the geometrical shape of the object is simple. However, for high frequency radar systems, the received signal can be modeled approximately by a sum of signals received from some dominant and discrete scattering points on the target. These scattering points provide a concise and useful description of the object for the target recognition [3].

Without loss of generality and neglecting the envelope of the transmitted signal, it is assumed that the radar transmits a signal, which may be written as

$$s_{tx}(t) = \exp(j2\pi f_0 t) \quad (1)$$

where  $f_0$  is the radar carrier frequency. The generic received signal can be written as

$$s_{rx}(t) = \sum_{i=0}^{N_s-1} \mu_i(t) \exp(j2\pi f_0(t - \tau_i(t))) \quad (2)$$

where  $N_s$  is the number of scattering points,  $\tau_i(t)$  and  $\mu_i(t)$  are the delay of propagation and the occlusion function of the  $i$ th scatterer, respectively. This latter is a binary function whose possible values are  $\{0, 1\}$ . This function usually depends on the aspect angle  $\alpha(t)$ , that is the angle between

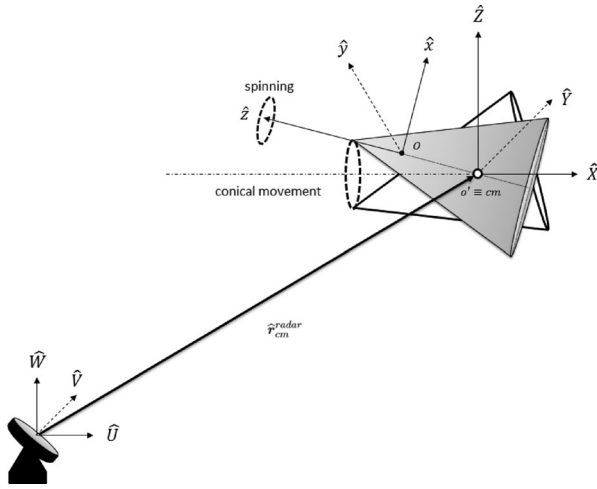


Fig. 1. Reference systems for ballistic targets.

the radar LOS (line of sight) and the symmetry axis of the target. Its value is 1 when there is a LOS for the scattering points, and 0 otherwise. An expression of the propagation delay for the generic point is given by

$$\tau_i(t) = \frac{2\rho_i(t)}{c} \quad (3)$$

where  $c = 3 \times 10^8$  m/s represents the speed of light in vacuum and  $\rho_i(t)$  is the distance between the radar and the considered point.

Considering three reference systems, as Fig. 1 illustrates: the principal reference system  $(\hat{U}, \hat{V}, \hat{W})$ , centered on the radar; the natural coordinate system  $(\hat{X}, \hat{Y}, \hat{Z})$ , which is parallel to the previous one and whose origin is the center of mass of the target; the local system  $(\hat{x}, \hat{y}, \hat{z})$  such that the axis  $\hat{z}$  corresponds with the symmetry axis of target [2].

The distance  $\rho_i(t)$  is the norm of the position vector  $\mathbf{r}_i^{\text{radar}}$ , i.e.,

$$\rho_i(t) = \|\mathbf{r}_i^{\text{radar}}\| = \|\mathbf{r}_{cm}^{\text{radar}} + \mathbf{v}t + \mathbf{r}_i(t)\| \quad (4)$$

where  $\mathbf{r}_{cm}^{\text{radar}}$  is the initial position vector of the mass center with respect to the system  $(\hat{U}, \hat{V}, \hat{W})$ ,  $\mathbf{v}$  is the translation velocity of the target and  $\mathbf{r}_i(t)$  is the position of the considered point with respect to the  $(\hat{X}, \hat{Y}, \hat{Z})$  system.

Neglecting the time dependence for conciseness,  $\mathbf{r}_i$  can be written as the following column vector

$$\mathbf{r}_i = (X_t, Y_t, Z_t)^T = \mathbf{T}_m \mathbf{R}_{t_0} (\mathbf{r}_p^{\text{local}} - \mathbf{r}_{cm}^{\text{local}}) \quad (5)$$

where  $(\cdot)^T$  is the transpose operator,  $\mathbf{R}_{t_0}$  is the Euler matrix that sets the position of the target with respect to the second system  $(\hat{X}, \hat{Y}, \hat{Z})$  at the initial time instant  $t_0$ ,  $\mathbf{T}_m = \mathbf{T}_m(t)$  is the matrix depending on the micromotions made by the object, while  $\mathbf{r}_p^{\text{local}}$  and  $\mathbf{r}_{cm}^{\text{local}}$  are, respectively, the positions in the local system of the generic point and center of mass [2], [4].

## A. BM Warhead

Evaluating the case of a conical warhead, three dominant points of scattering are usually considered. The first coincides with the tip of the cone, the others two correspond to the intersection between the base of the cone and the plane given by the radar LOS and the target symmetry axis. However, for warheads with fins, other points need to be considered, namely the tips of the fins. Therefore, assuming a simple conical warhead, the expression of the received signal is

$$s_{rx}(t) = \sum_{i=0}^2 \mu_i(t) \exp \left\{ j2\pi f_0 \left( t - \frac{2\rho_i(t)}{c} \right) \right\} \quad (6)$$

where  $\rho_i(t)$  depends on the micromotion matrix according to (4) and (5). In the case of conical warheads, the matrix  $\mathbf{T}_m$  is given by the product of three terms, namely

$$\mathbf{T}_m = \mathbf{R}_c \mathbf{R}_s \mathbf{R}_n \quad (7)$$

where the matrices  $\mathbf{R}_c$  and  $\mathbf{R}_s$  depend on conical movement and spinning, which together make up the precession, while  $\mathbf{R}_n$  depends on nutation. Since the matrices  $\mathbf{R}_c$  and  $\mathbf{R}_s$  are related to rotation movements, they can be obtained by the Rodrigues formula [2], [25]

$$\begin{aligned} \mathbf{R}_c &= \mathbf{I} + \hat{\mathbf{E}} \sin(\Omega_c t) + \hat{\mathbf{E}}^2 (1 - \cos(\Omega_c t)) \\ \mathbf{R}_s &= \mathbf{I} + \hat{\mathbf{E}} \sin(\Omega_s t) + \hat{\mathbf{E}}^2 (1 - \cos(\Omega_s t)) \end{aligned} \quad (8)$$

where  $\mathbf{I}$  is the identity matrix of dimension  $3 \times 3$ ,  $\Omega_c = |\mathbf{w}_c|$  and  $\Omega_s = |\mathbf{w}_s|$ , where  $\mathbf{w}_c$  and  $\mathbf{w}_s$  are the rotation angular velocity vectors of conical movement and spinning, respectively, while  $\hat{\mathbf{E}}_c$  and  $\hat{\mathbf{E}}_s$  represent the *skew symmetric matrixs* [2] obtained by normalized vectors  $\mathbf{w}_c$  and  $\mathbf{w}_s$ .

In order to evaluate the matrix  $\mathbf{R}_n$ , a new coordinate system  $(\hat{x}_n, \hat{y}_n, \hat{z}_n)$  has to be considered. The unit directional vector that identifies the symmetry axis of the conical warhead with respect to the principal system  $(\hat{X}, \hat{Y}, \hat{Z})$  is defined as follows

$$\hat{\mathbf{z}}_{t_0} = \mathbf{R}_{t_0} \mathbf{a}_0 \quad (9)$$

where  $\mathbf{a}_0 = (0, 0, 1)^T$ . Due to the precession, the coordinates of target axis depend on time for its rotation during the conical motion, namely

$$\hat{\mathbf{z}}_t = \mathbf{R}_c \mathbf{R}_{t_0} \mathbf{a}_0 \quad (10)$$

where  $\hat{\mathbf{z}}_t$  represents the unit directional vector at time instant  $t$ . Considering the cone axis oscillating in the plane given by  $\widehat{O'C}$  (see Fig. 2) and  $\hat{\mathbf{z}}_t$ , the new reference system  $(\hat{x}_n, \hat{y}_n, \hat{z}_n)$  is chosen so that  $\hat{x}_n$  coincides with the precession axis while the  $\hat{z}_n$  axis is perpendicular to the oscillation plane, as shown in Fig. 2.

Therefore, the expressions of the three unit directional vectors of the system are

$$\hat{\mathbf{x}}_n = \frac{\widehat{O'C}}{\|\widehat{O'C}\|}, \quad \hat{\mathbf{z}}_n = \frac{\widehat{O'C} \times \hat{\mathbf{z}}_t}{\|\widehat{O'C} \times \hat{\mathbf{z}}_t\|}, \quad \hat{\mathbf{y}}_n = \frac{\hat{\mathbf{x}}_n \times \hat{\mathbf{z}}_n}{\|\hat{\mathbf{x}}_n \times \hat{\mathbf{z}}_n\|}. \quad (11)$$

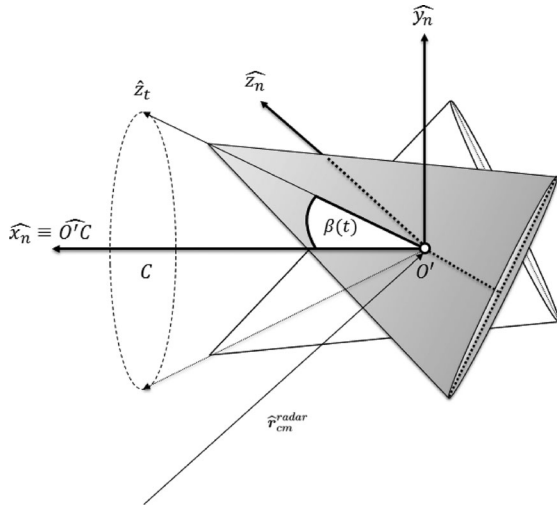


Fig. 2. The reference system  $(\hat{x}_n, \hat{y}_n, \hat{z}_n)$ .

Considering the three unit directional vectors  $(\hat{x}, \hat{y}, \hat{z})$  of the system  $(\hat{X}, \hat{Y}, \hat{Z})$ , the transition matrix  $A_n$ , which represents the relationship between the previous and the new system, is given by

$$(\hat{x}_n, \hat{y}_n, \hat{z}_n) = (\hat{x}, \hat{y}, \hat{z}) A_n. \quad (12)$$

Since the reference coordinates  $(\hat{X}, \hat{Y}, \hat{Z})$  are the natural coordinates, which means that  $(\hat{x}, \hat{y}, \hat{z})$  form a  $3 \times 3$  identity matrix, then matrix  $A_n$  is obtained as follows

$$A_n = (\hat{x}_n, \hat{y}_n, \hat{z}_n) \quad (13)$$

from which it is clear that the transition matrix is orthonormal. Therefore, the position vector of a generic point in the new reference system at initial time instant  $t_0$  is

$$\mathbf{r}_{n_p}(t_0) = (x_{n_p}(t_0), y_{n_p}(t_0), z_{n_p}(t_0))^T = A_n^{-1} \mathbf{r}_p(t_0). \quad (14)$$

Considering the case of a sinusoidal oscillation of the precession angle, which is given by  $\beta(t)$  (as shown in Fig. 2), then

$$\Delta\beta(t) = \beta_n \sin(\omega_n t) = \beta_n \sin(2\pi f_n t) \quad (15)$$

where  $f_n$  and  $\beta_n$  represent the frequency and maximum value of the oscillation, respectively. Since in the new reference system the oscillation of the cone axis is a rotation around the  $\hat{z}_n$  axis, the position vector  $\mathbf{r}_{n_p}(t)$  at the instant  $t$  is

$$\mathbf{r}_{n_p}(t) = \mathbf{B}_n \mathbf{r}_{n_p}(t_0) = \mathbf{B}_n A_n^{-1} \mathbf{r}_p(t_0) \quad (16)$$

where  $\mathbf{B}_n$  is the Euler rotation matrix around  $\hat{z}_n$  axis given by

$$\mathbf{B}_n = \begin{bmatrix} \cos(\Delta\beta) & -\sin(\Delta\beta) & 0 \\ \sin(\Delta\beta) & \cos(\Delta\beta) & 0 \\ 0 & 0 & 1 \end{bmatrix}. \quad (17)$$

The position vector in the natural coordinates system is given by

$$\mathbf{r}_t = A_n \mathbf{r}_{n_t} = A_n \mathbf{B}_n A_n^{-1} \mathbf{r}_{t_0}. \quad (18)$$

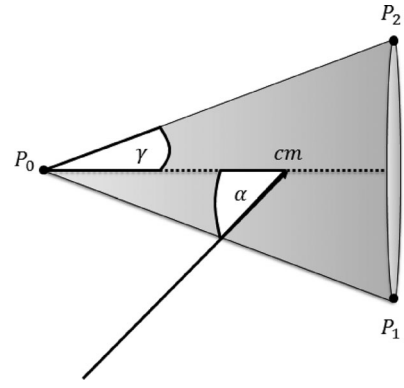


Fig. 3. Representation of three principal scattering points of conical warhead.

TABLE I

Value of the Occlusion Function  $\mu_i(t)$  for the Three Principal Scattering Points  $P_0, P_1$ , and  $P_2$  With Respect to the Aspect Angles  $\alpha$

	$\alpha < \gamma$	$\gamma \leq \alpha < \frac{\pi}{2} - \gamma$	$\frac{\pi}{2} - \gamma \leq \alpha < \frac{\pi}{2}$	$\frac{\pi}{2} \leq \alpha < \pi - \gamma$	$\pi - \gamma \leq \alpha \leq \pi$
$\mu_0(\alpha)$	1	1	1	1	0
$\mu_1(\alpha)$	1	1	1	1	1
$\mu_2(\alpha)$	1	0	0	1	1

Finally, the nutation matrix  $\mathbf{R}_n$  can be written as

$$\mathbf{R}_n = A_n \mathbf{B}_n A_n^{-1}. \quad (19)$$

The occlusion function  $\mu_i(t)$  depends only on the aspect angle  $\alpha(t)$  and the semiangle  $\gamma$  that defines the cone shown in Fig. 3. The functions  $\mu_i(t)$ , with  $i = 0, 1, 2$ , are evaluated for  $\alpha(t) \in [0, \pi]$  due to the symmetric shape of the target and to the specific micromovements exhibited by warheads. Specifically, for the tip of the cone identified with  $P_0$ , the occlusion function  $\mu_i(t) = 0$  for  $\alpha(t) \geq \pi - \gamma$ , which means that in this interval occlusion occurs. For the scattering point  $P_1$ , which is one of the points on the cone base at minimum distance from the radar, occlusion never occurs, so the function  $\mu_i(t) = 1$  for all values of  $\alpha(t)$ . On the other hand for the point  $P_2$  occlusion occurs when  $\alpha(t) \in [\gamma, \frac{\pi}{2}]$ . The interval of occlusion for several scattering points are summarized in Table I.

Let us now consider the warheads with fins then the received signal can be modeled as follows:

$$s_{rx}(t) = \sum_{i=0}^2 \mu_i(t) \exp \left\{ j2\pi f_0 \left( t - \frac{2\rho_i t}{c} \right) \right\} + \sum_{a=1}^{N_{\text{fin}}} \mu_a(t) \exp \left\{ j2\pi f_0 \left( t - \frac{2\rho_a t}{c} \right) \right\} \quad (20)$$

where  $N_{\text{fin}}$  is the number of fins and  $\mu_a(t)$  is the occlusion function for the  $a$ th fin. In the presence of fins, the occlusion function does not only depend on the aspect angle  $\alpha$ , but also on the spinning of the cone as it can cause the fins to be occluded behind the warhead body. In order to evaluate the occlusion function for the fins, the physical optics approximation is considered. This is a valid approx-

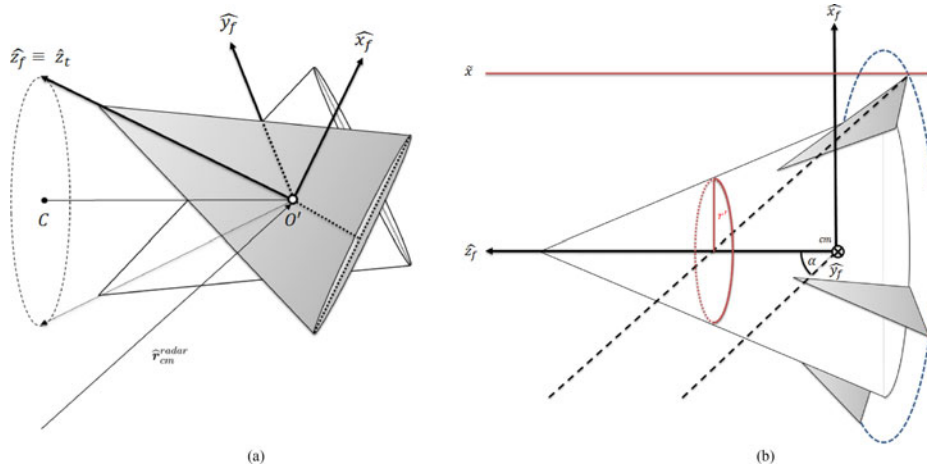


Fig. 4. (a) Reference system  $(\hat{x}_f, \hat{y}_f, \hat{z}_f)$ . (b) Representation of the threshold  $\tilde{x}$ .

imation given the high frequency at which the radar system operates. Since the targets of interest are within the Fraunhofer zone [2], the rays that strike the targets can be considered as parallel. The occlusion of fins can only occur for values of the aspect angle such that  $\alpha(t) \geq \gamma_{fin}$ , where  $\gamma_{fin}$  is the semiangle of an isosceles triangle whose height is equal to the height of the cone and the base is equal to the diameter of circumference drawn by rotating fins. Therefore, the function  $\mu_a(t) = 1$  when  $\alpha(t) \in [0, \gamma_{fin}]$ . In order to evaluate  $\mu_a(t)$  for  $\alpha(t) \geq \gamma_{fin}$ , a new reference system  $(\hat{x}_f, \hat{y}_f, \hat{z}_f)$  has to be considered, as shown in Fig. 4(a). The reference system is chosen in order to have the  $\hat{z}_f$  axis coincident with the cone axis, while  $\hat{y}_f$  is perpendicular to the plane given by the radar LOS and the cone axis

$$\hat{z}_f = \hat{z}_t, \quad \hat{y}_f = \frac{\hat{z}_f \times \hat{\mathbf{r}}_{cm}^{radar}}{\|\hat{z}_f \times \hat{\mathbf{r}}_{cm}^{radar}\|}, \quad \hat{x}_f = \frac{\hat{y}_f \times \hat{z}_f}{\|\hat{y}_f \times \hat{z}_f\|}. \quad (21)$$

Since the reference system  $(\hat{X}, \hat{Y}, \hat{Z})$  is the natural coordinate system, the transition matrix  $\mathbf{A}_f$  is given by

$$\mathbf{A}_f = (\hat{\mathbf{x}}_f, \hat{\mathbf{y}}_f, \hat{\mathbf{z}}_f). \quad (22)$$

The position vector of the  $a$ th fin tip in the new system is given by

$$\mathbf{r}_{fa} = (x_{fa}, y_{fa}, z_{fa})^T = \mathbf{A}_f^{-1} \mathbf{r}_a \quad (23)$$

where  $\mathbf{r}_a$  is the position vector in the natural system. The value of occlusion function for  $\alpha(t) \geq \gamma_{fin}$  is calculated by comparing the coordinate  $x_{fa}$  with a suitable threshold as follows

$$\mu_a(t) = \begin{cases} 1 & \text{if } x_{fa} < \tilde{x} \\ 0 & \text{if } x_{fa} \geq \tilde{x} \end{cases}. \quad (24)$$

In order to evaluate the threshold  $\tilde{x}$  it is necessary to calculate when the straight line joining the radar and tip of the fin becomes tangential to the cone surface [see Fig. 4(b)].

Considering the reference system  $(\hat{x}_{f_0}, \hat{y}_{f_0}, \hat{z}_{f_0})$  obtained moving the origin of system  $(\hat{x}_f, \hat{y}_f, \hat{z}_f)$  into center of cone bottom as shown in Fig. 5, the position vectors of

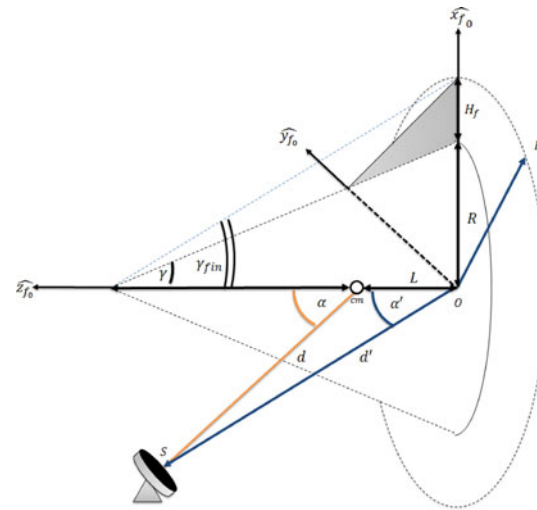


Fig. 5. Reference system  $(\hat{x}_{f_0}, \hat{y}_{f_0}, \hat{z}_{f_0})$ .

the fin tip  $\overline{OF}$ , and of the radar  $\overline{OS}$  are

$$\begin{aligned} \overline{OF} &= [(R + H_f) \cos(\phi), (R + H_f) \sin(\phi), 0]^T \\ \overline{OS} &= [-d' \sin(\alpha'), 0, d' \cos(\alpha')]^T \end{aligned} \quad (25)$$

where  $R$  is the bottom radius of the cone,  $H_f$  is the fin height,  $\phi$  is the angle between the fin and  $\hat{x}_{f_0}$  axis, and where

$$\alpha' = \tan^{-1} \left( \frac{d \sin(\alpha)}{d \cos(\alpha) + L} \right) \quad (26)$$

$$d' \simeq d + L \cos(\alpha') \quad (27)$$

with  $\alpha$  the aspect angle,  $d = \|\mathbf{r}_{cm}^{radar}\|$  the distance between the radar and the mass center, and  $L$  the distance between the mass center and the bottom center of the cone.

The conical surface is represented by the function:

$$\begin{aligned} f(x_{f_0}, y_{f_0}, z_{f_0}) &= r^2 - (x_{f_0}^2 + y_{f_0}^2) \\ &= R^2 \left( 1 - \frac{z_{f_0}}{H} \right)^2 - (x_{f_0}^2 + y_{f_0}^2) \end{aligned} \quad (28)$$

where  $r' = r'(z_{f_0})$  is the radius of the generic cone section given by

$$r'(z_{f_0}) = R \left(1 - \frac{z_{f_0}}{H}\right) \quad (29)$$

where  $H$  is the cone height. Considering the generic point of the cone  $P$  whose position vector is

$$\overline{OP} = \left[ r' \cos(\psi), r' \sin(\psi), H \left(1 - \frac{r'}{R}\right) \right]^T \quad (30)$$

where  $\psi$  is the position angle with respect to  $\widehat{x}_{f_0}$  axis, the lines from  $P$  to  $F$  and  $S$  are

$$\begin{aligned} \overline{PF} &= \overline{OP} - \overline{OF} = \left[ r' \cos(\psi) - (R + H_f) \cos(\phi), r' \right. \\ &\quad \left. \sin(\psi) - (R + H_f) \sin(\phi), H \left(1 - \frac{r'}{R}\right) \right]^T \\ \overline{PS} &= \overline{OP} - \overline{OS} = \left[ r' \cos(\psi) + d' \sin(\alpha'), r' \sin(\psi), \right. \\ &\quad \left. H \left(1 - \frac{r'}{R}\right) - d' \cos(\alpha') \right]^T \end{aligned} \quad (31)$$

respectively. In order to evaluate the occlusion threshold, it is necessary to evaluate the angle  $\phi$  and  $\psi$  such that  $\overline{PF}$  and  $\overline{PS}$  are both tangent to the conical surface as follows

$$\begin{cases} \left[ \frac{\partial f}{\partial x_{f_0}}, \frac{\partial f}{\partial y_{f_0}}, \frac{\partial f}{\partial z_{f_0}} \right]^T \cdot \overline{PF} = 0 \\ \left[ \frac{\partial f}{\partial x_{f_0}}, \frac{\partial f}{\partial y_{f_0}}, \frac{\partial f}{\partial z_{f_0}} \right]^T \cdot \overline{PS} = 0 \end{cases} \quad (32)$$

where the components of gradient vector for a generic cone point are evaluated from (28) as

$$\begin{aligned} \frac{\partial f}{\partial x_{f_0}} &= -2x_{f_0} = -2r' \cos(\psi); \\ \frac{\partial f}{\partial y_{f_0}} &= -2y_{f_0} = -2r' \sin(\psi); \\ \frac{\partial f}{\partial z_{f_0}} &= \frac{-2R^2}{H} \left(1 - \frac{z_{f_0}}{H}\right) = \frac{-2Rr'}{H}; \end{aligned} \quad (33)$$

with

$$x_{f_0} = r' \cos(\psi); \quad y_{f_0} = r' \sin(\psi); \quad z_{f_0} = H \left(1 - \frac{r'}{R}\right). \quad (34)$$

From (32) and (33) follows

$$\begin{cases} (-2r') \left( r' \cos^2(\psi) - (R + H_f) \cos(\psi) \cos(\phi) \right. \\ \quad \left. + r' \sin^2(\psi) - (R + H_f) \sin(\psi) \sin(\phi) - r' + R \right) = 0 \\ (-2r') \left( d' \sin(\alpha') \cos(\psi) + r' \cos^2(\psi) + r' \sin^2(\psi) \right. \\ \quad \left. + R - r' - \frac{Rd' \cos(\alpha')}{H} \right) = 0 \end{cases} \quad (35)$$

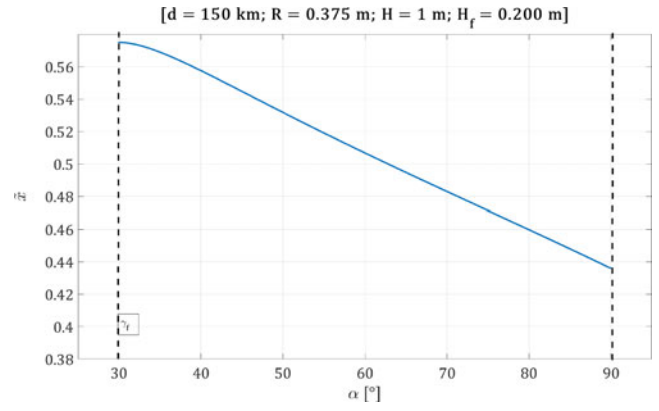


Fig. 6. Example of threshold values  $\tilde{x}$  as a function of aspect angle ( $\alpha$ ).

which leads to

$$\begin{cases} \cos(\psi - \phi) = \frac{R}{R + H_f} \\ \cos(\psi) = \left[ \frac{d \cos(\alpha') R}{H} - R \right] \frac{1}{d \sin(\alpha')} = \left[ \frac{\tan(\gamma)}{\tan(\alpha')} - \frac{R}{d \sin(\alpha')} \right]. \end{cases} \quad (36)$$

$\forall r' > 0$

Finally, the threshold is given by

$$\tilde{x} = (H_f + R) \cos(\phi) \quad (37)$$

where

$$\phi = \cos^{-1} \left[ \frac{\tan(\gamma)}{\tan(\alpha')} - \frac{R}{d \sin(\alpha')} \right] - \cos^{-1} \left[ \frac{R}{R + H_f} \right]. \quad (38)$$

Fig. 6 shows how the threshold values varies as a function of aspect angle for the cone dimensions  $H$  and  $R$  of 1 and 0.375 m, respectively, fin height  $H_f = 0.200$  m and at a distance of 150 km. It has to be pointed out that  $\tilde{x}$  depends on the distance between the target and radar, which makes this general model valid also for distances relatively small, e.g., in the case of an on-board radar of an interceptor.

## B. Confusing Object

In the case of confusing objects, according to (2), the received signal is given by

$$s_{rx}(t) = \sum_{i=0}^{N_d} \mu_i(t) \exp \left\{ j 2\pi f_0 \left( t - \frac{2\rho_i t}{c} \right) \right\} \quad (39)$$

where  $N_d$  is the number of scatterers. Since the confusing objects only wobble, and assuming for simplicity that the angular rotation vector is perpendicular to the plane given by the symmetry axis of the objects and the radar LOS, the matrix  $\mathbf{T}_m$  is given by Rodrigues formula [2], [25]

$$\mathbf{T}_m = \mathbf{T}_r = \mathbf{I} + \hat{\mathbf{E}} \sin(\Omega_r t) + \hat{\mathbf{E}}^2 (1 - \cos(\Omega_r t)) \quad (40)$$

where  $\Omega_r = |\mathbf{w}_r|$  and  $\mathbf{w}_r$  is the angular rotation velocity vector, while  $\hat{\mathbf{E}}$  is the skew symmetric matrix obtained by the normalized vector  $\mathbf{w}_r$  [2]. Moreover, the number of dominant scattering points depends on the type and geometry of confusing object. In particular, for a sphere, two diametrically opposite scatterers are chosen on the circumference given by the intersection between the plane given by

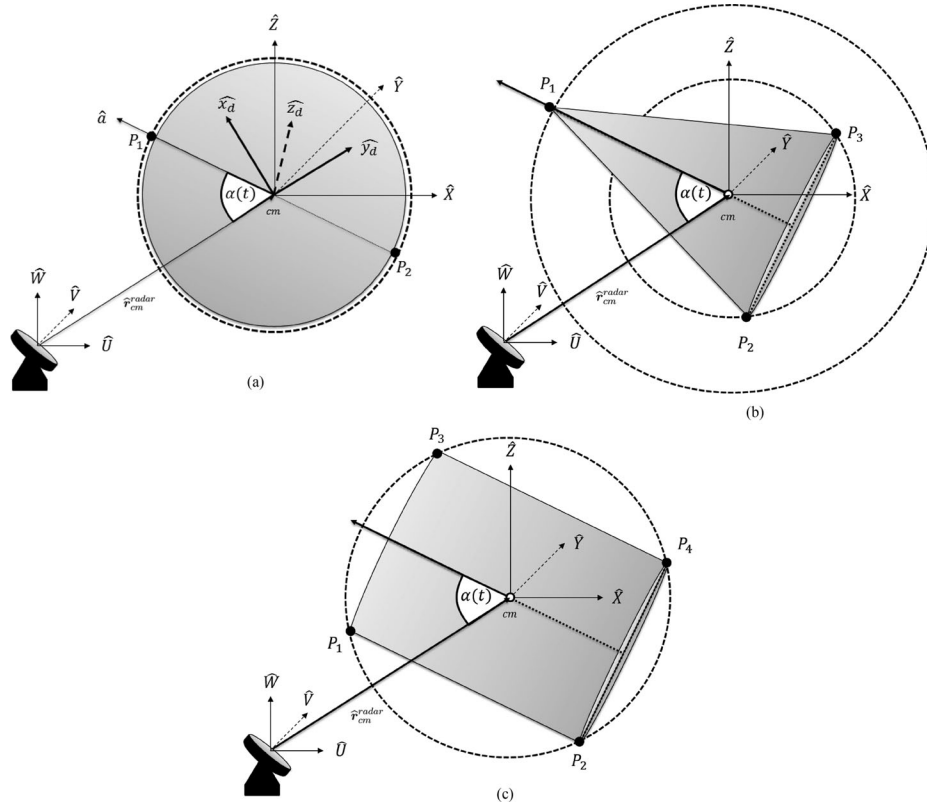


Fig. 7. Representation of the scattering points of confusing objects. (a) Sphere. (b) Cone. (c) Cylinder.

the symmetry axis of the object and the radar LOS and the sphere. In order to evaluate the phenomenon of occlusion for the spherical object, a new reference system  $(\hat{x}_d, \hat{y}_d, \hat{z}_d)$  is considered, as illustrated in Fig. 7(a). Assuming that the sphere axis  $\hat{a}_d$  is the line passing through the two scatterers, the  $\hat{y}_d$  axis is chosen so as to be parallel to the radar LOS, while the  $\hat{z}_d$  axis is perpendicular to the plane identified by the radar LOS and the sphere axis, as illustrated in Fig. 7(a). Therefore, the unit directional vectors of the system are given by

$$\hat{y}_d = \frac{\hat{r}_{cm}^{\text{radar}}}{\|\hat{r}_{cm}^{\text{radar}}\|}, \quad \hat{z}_d = \frac{\hat{a}_d \times \hat{r}_{cm}^{\text{radar}}}{\|\hat{a}_d \times \hat{r}_{cm}^{\text{radar}}\|}, \quad \hat{x}_d = \frac{\hat{y}_d \times \hat{z}_d}{\|\hat{y}_d \times \hat{z}_d\|}. \quad (41)$$

Since the reference system  $(\hat{X}, \hat{Y}, \hat{Z})$  is the natural reference system, the transition matrix  $A_d$  between the two systems is

$$A_d = (\hat{x}_d, \hat{y}_d, \hat{z}_d). \quad (42)$$

The position vector of the  $i$ th scattering point in the new reference system is given by

$$\mathbf{r}_{d_i} = (x_{d_i}, y_{d_i}, z_{d_i})^T = A_d^{-1} \mathbf{r}_i \quad (43)$$

where  $\mathbf{r}_i$  is the position vector in the natural reference system. Furthermore, the occlusion for the scatterers occurs when the coordinate  $y_{d_i} > 0$ , so it follows

$$\mu_i(t) = \begin{cases} 1 & \text{if } y_{d_i} \leq 0 \\ 0 & \text{if } y_{d_i} > 0 \end{cases}. \quad (44)$$

As for the warhead, three scatterers are considered for the conical object, namely the tip of the cone and the two on the base in proximity of the plane given by target symmetry axis and the radar LOS, as shown in Fig. 7(b). However, because of the different motion of the confusing object compared to the warhead, the occlusion of the three points is evaluated for values of the aspect angle which lays in  $[0, 2\pi]$ . In particular,  $\mu_i(t) = 0$  for the following:

- 1)  $P_1$  when  $\alpha(t) \in [\pi - \gamma, \pi + \gamma]$ ;
- 2)  $P_2$  when  $\alpha(t) \in \left[\frac{3\pi}{2}, 2\pi - \gamma\right]$ ;
- 3)  $P_3$  when  $\alpha(t) \in \left[\gamma, \frac{\pi}{2}\right]$ .

Finally, for cylindrical objects four scatterers are considered: two for each base of the cylinder and on the plane given by target symmetry axis and the radar LOS. As for the conical object, the occlusion function for these points depends only on the aspect angle, specifically  $\mu_i(t) = 0$  for the following:

- 1)  $P_1$  when  $\alpha(t) \in \left[\pi, \frac{3\pi}{2}\right]$ ;
- 2)  $P_2$  when  $\alpha(t) \in \left[\frac{3\pi}{2}, 2\pi\right]$ ;
- 3)  $P_3$  when  $\alpha(t) \in \left[\frac{\pi}{2}, \pi\right]$ ;
- 4)  $P_4$  when  $\alpha(t) \in \left[0, \frac{\pi}{2}\right]$ .

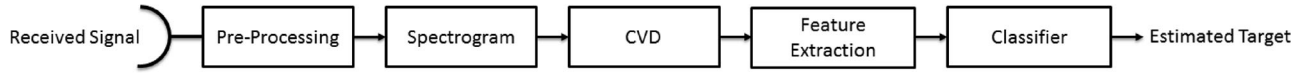


Fig. 8. Block diagram of the proposed algorithm.

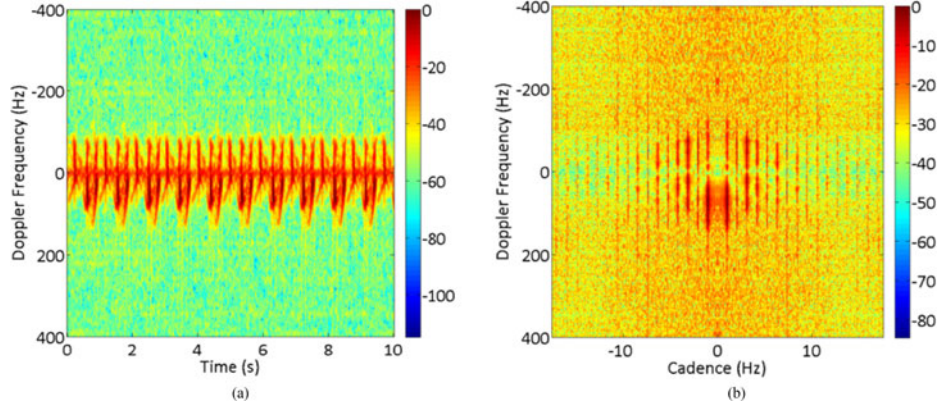


Fig. 9. Example of spectrogram and CVD obtained by a received signal from a cylindrical object. (a) Spectrogram. (b) CVD.

Fig. 7(c) shows the scattering points considered for a cylindrical object and their circular trajectory during its flight.

### III. FEATURE EXTRACTION ALGORITHM

In this section, the algorithm to extract micro-Doppler-based features for the classification of ballistic targets is described. Fig. 8 shows a block diagram of the classification method outlining the common steps for the three different approaches proposed in this paper. The starting point of the proposed algorithm is the received signal  $\tilde{s}_{rx}(n)$ , with  $n = 0, \dots, N$ , containing micro-Doppler components and comprising of  $N$  signal samples. The received signal has to be preprocessed before the evaluation of the micro-Doppler signature. The first block includes a notch filtering, down-sampling, and normalization (as required for the pZ-based method). The second step is the spectrogram computation of the preprocessed signal  $\tilde{s}_{rx}(n)$

$$\chi(v, k) = \left| \sum_{n=0}^{N-1} \tilde{s}_{rx}(n) w_h(n-k) \exp\left(-j2\pi v \frac{n}{N}\right) \right|, \quad k = 0, \dots, K-1 \quad (45)$$

where  $v$  is the normalized frequency and  $w_h(\cdot)$  is the smoothing window. The spectrogram is a TFD that allows the signal frequency time variations to be evaluated and it is chosen for its robustness with respect to the production of artefacts. In Fig. 9(a), the spectrogram obtained by a signal scattered from a cylindrical object is shown. Observing Fig. 8, the next step consists in the extraction of the CVD, that is defined as the Fourier transform of the spectrogram along each frequency bin [5]:

$$\Delta(v, \varepsilon) = \left| \sum_{k=0}^{K-1} \chi(v, k) \exp\left(-j2\pi \varepsilon \frac{k}{K}\right) \right| \quad (46)$$

where  $\varepsilon$  is known as the cadence frequency. The CVD is chosen because it offers the possibility of using, as discriminants, the cadence of each frequency component and the maximum Doppler shift, and because the CVD is more robust than the spectrogram since it does not depend on the initial phase of moving objects. In Fig. 9(b), the CVD obtained from the spectrogram given in Fig. 9(a) is shown, in which it is possible to see that the zero cadence component is filtered out. Finally, the CVD has to be processed to extract a  $Q$ -dimensional feature vector  $\mathbf{F} = [F_0, F_1, \dots, F_{Q-1}]$ , which can identify unequivocally each class. The feature extraction block of Fig. 8 for the three different approaches will be described in the following sections. Before classification, the vector  $\mathbf{F}$  is normalized as follows

$$\tilde{\mathbf{F}} = \frac{\mathbf{F} - \eta_{\mathbf{F}}}{\sigma_{\mathbf{F}}} \quad (47)$$

where  $\eta_{\mathbf{F}}$  and  $\sigma_{\mathbf{F}}$  are the statistical mean and standard deviation of the vector  $\mathbf{F}$ , respectively.

The classification performances of the extracted feature vectors are evaluated using the  $k$ -Nearest neighbor ( $k$ NN) classifier, modified in order to account for *unknown* class. In particular, let  $\mathcal{T}$  be the training vectors set, for each class  $v$  an hypersphere  $\mathcal{S}_{\mathbf{CM}_v}(\zeta_v)$  is considered, with center  $\mathbf{CM}_v$  and radius  $\zeta_v$ . In the case in which the tested vector does not belong to any hypersphere, it is declared as unknown. The operation mode of this classifier is composed by three phases. In the first phase, the set  $\mathcal{N}$  of nearest neighbor training vectors to the tested vector  $\mathbf{F}$  is selected from  $\mathcal{T}$  as follows

$$\mathcal{N} = \{\tilde{\mathbf{F}}_1, \dots, \tilde{\mathbf{F}}_k : \forall i = 1, \dots, k, \|\tilde{\mathbf{F}}_i - \mathbf{F}\| < \min_{\tilde{\mathbf{F}} \in \{\mathcal{T} - \tilde{\mathbf{F}}_1, \dots, \tilde{\mathbf{F}}_{i-1}\}} \|\tilde{\mathbf{F}} - \mathbf{F}\|\}. \quad (48)$$

The second phase consists into definition of vector  $\boldsymbol{\iota}$  whose elements represent a label for each vector in  $\mathcal{N}$ . Each label



can assume an integer value in the range  $[0, V]$ , where  $V$  is the number of possible classes. The value 0 is assigned when the tested vector does not belong to any hypersphere of the vectors in  $\mathcal{N}$ , while the values  $[1, V]$  correspond to a specific class. Specifically,  $\forall i = 1, \dots, k$ , the  $i$ -label  $t_i$  is updated as follows

$$t_i = \begin{cases} 0 & \|\tilde{\mathbf{F}}_i - \mathbf{F}\| > \zeta_v \\ v & \text{otherwise} \end{cases} \quad (49)$$

where  $v$  is the value corresponding to the belonging class of  $\tilde{\mathbf{F}}_i$ . Finally, the  $(V + 1)$ -dimensional score vector  $\mathbf{s}$  is evaluated, whose elements are the occurrences, normalized to  $k$ , of the integers  $[0, \dots, V]$  in the vector  $\mathbf{t}$ . The estimation rule then may be implemented as follows:

$$\hat{v} = \begin{cases} \arg \max_v \mathbf{s} & \text{if } \max(\mathbf{s}) > \frac{1}{2} \\ 0 & \text{otherwise} \end{cases} \quad (50)$$

where 0 is the unknown class.

Assuming that the feature vectors of each class are distributed uniformly around their mean vector, for all the Monte Carlo runs, the hypersphere radius  $\zeta_v$  was chosen equal to  $\sigma_v \sqrt{12}/2$ , where  $\sigma_v = \text{tr}(\mathbf{C}_v)$  and  $\mathbf{C}_v$  is the covariance matrix of the training vectors which belong to the class  $v$ . The choice is made according to the statistical proprieties of uniform distributions. In fact, for one-dimensional (1-D) uniform variables, the sum of mean and the product between the standard deviation and the factor  $\sqrt{12}/2$  gives the maximum possible value of the distribution. The choice of a  $k$ NN classifier is justified for its low computational load and its capability of providing score values as an output. However, in general other classifiers with similar characteristics could also be selected. The selection of the best classifier is outside the scope of this paper.

#### A. ACVD-Based Feature Vector Approach

In the ACVD-based feature vector approach, seven features are computed from the ACVD. The starting point is the mean of the CVD along each cadence bin; the resulting 1-D function is then normalized to have a unit area. From the resulting function  $\check{\Delta}(n)$ ,  $n = 0, \dots, N_c - 1$ , where  $N_c$  is the number of cadence bins, four statistical indices are extracted :

(1) Mean:

$$F_0 = \frac{1}{N_c} \sum_{n=0}^{N_c-1} \check{\Delta}(n). \quad (51)$$

(2) Standard deviation:

$$F_1 = \sqrt{\frac{1}{N_c - 1} \sum_{n=0}^{N_c-1} \left[ \check{\Delta}(n) - \frac{1}{N_c} \sum_{n=0}^{N_c-1} \check{\Delta}(n) \right]^2}. \quad (52)$$

(3) Kurtosis:

$$F_2 = \frac{\frac{1}{N_c} \sum_{n=0}^{N_c-1} \left[ \check{\Delta}(n) - \frac{1}{N_c} \sum_{n=0}^{N_c-1} \check{\Delta}(n) \right]^4}{\left( \sqrt{\frac{1}{N_c-1} \sum_{n=0}^{N_c-1} \left[ \check{\Delta}(n) - \frac{1}{N_c} \sum_{n=0}^{N_c-1} \check{\Delta}(n) \right]^2} \right)^4} - 3. \quad (53)$$

(4) Skewness:

$$F_3 = \frac{\frac{1}{N_c} \sum_{n=0}^{N_c-1} \left[ \check{\Delta}(n) - \frac{1}{N_c} \sum_{n=0}^{N_c-1} \check{\Delta}(n) \right]^3}{\left( \sqrt{\frac{1}{N_c-1} \sum_{n=0}^{N_c-1} \left[ \check{\Delta}(n) - \frac{1}{N_c} \sum_{n=0}^{N_c-1} \check{\Delta}(n) \right]^2} \right)^3}. \quad (54)$$

Three other indices, specifically the peak sidelobe level (PSL) ratio and two different definitions of the integrated sidelobe level (ISL) ratio, are computed from the normalized autocorrelation of the sequence  $\check{\Delta}(n)$ ,  $C_{\check{\Delta}}(m)$ ,  $m = 0, \dots, M - 1$ . Specifically

$$F_4 = \text{PSL} = \max_m \frac{|C_{\check{\Delta}}(m)|}{|C_{\check{\Delta}}(0)|} \quad (55)$$

while the latter are

$$F_5 = \text{ISL}_1 = \frac{\sum_{m=1}^{M-1} |C_{\check{\Delta}}(m)|}{|C_{\check{\Delta}}(0)|} \quad (56)$$

and

$$F_6 = \text{ISL}_2 = \frac{\sum_{m=1}^{M-1} |C_{\check{\Delta}}(m)|^2}{|C_{\check{\Delta}}(0)|} \quad (57)$$

respectively.

#### B. Pseudo-Zernike-Based Feature Vector Approach

The pZ moments of order  $r$  and repetition  $l$  of an image  $I(x, y)$ , introduced in [19], are geometric moments computed as the projection of the image on a basis of 2-D-polynomials which are defined on the unit circle. They are calculated as

$$\zeta_{r,l} = \frac{r+1}{\pi} \int_0^{2\pi} \int_0^1 W_{r,l}^*(\rho, \theta) I(\rho \cos \theta, \rho \sin \theta) \rho d\rho d\theta \quad (58)$$

where

$$W_{r,l}(\rho, \theta) = \sum_{h=0}^{r-|l|} \frac{\rho^{r-h} (-1)^h (2r+1-h)!}{h! (r+|l|+1-h)! (r-|l|-h)!} e^{jl\theta}, \quad (59)$$

with  $\rho \leq 1$ .

The moments have several properties, among which are that they are independent, since the pZ polynomials are orthogonal on the unit circle, and their modulus is rotational invariant.

The algorithm, proposed and tested in [18], computes  $(K + 1)^2$  pZ moments, where  $K$  is the maximum order (to be chosen by the user), by projecting the magnitude of the CVD on the pZ polynomials, and obtaining a feature vector

whose  $z$ th element is

$$F_z = \zeta_{r,l} \quad (60)$$

where  $r = l = 0, \dots, K - 1$  and  $z = 0, \dots, (k + 1)^2 - 1$ . Since the pZ moments are defined on the unit circle, the support of the spectrogram, hence that of the CVD, has to be chosen to be a unit square so that it can be inscribed in the unit circle [5], [18].

### C. Gabor Filter Based Feature Vector Approach

The 2-D Gabor function is the product of a complex exponential representing a sinusoidal plane wave and an elliptical 2-D Gaussian bell. Its analytical expression in the spatial domain, which can be normalized to have a compact form [22], [24], is

$$\psi(x, y) = \frac{f^2}{\pi\gamma\eta} e^{-\left(\frac{f^2}{\gamma^2}x^2 + \frac{f^2}{\eta^2}y^2\right)} e^{j2\pi f x'} \quad (61)$$

with

$$x' = x \cos(\theta) + y \sin(\theta) \quad \text{and} \quad y' = -x \sin(\theta) + y \cos(\theta) \quad (62)$$

where  $f$  is the central spatial frequency,  $\theta$  is the anticlockwise angle between the direction of the plain wave and the  $\hat{x}$ -axis,  $\gamma$  is the spatial width of the filter along the plane wave, and  $\eta$  is the spatial width perpendicular to the wave. Therefore, the sharpness of the filter is controlled on the major and minor axes by  $\eta$  and  $\gamma$ . The normalized expression of the Gabor function in the Fourier domain is [22]

$$\Psi(u, v) = e^{-\frac{\pi^2}{f^2}(\gamma^2(u-f)^2 + \eta^2 v^2)} \quad (63)$$

where

$$u' = u \cos(\theta) + v \sin(\theta) \quad \text{and} \quad v' = -u \sin(\theta) + v \cos(\theta). \quad (64)$$

In the proposed technique, as in the pZ moments based approach, the magnitude of the CVD, scaled to fit the unit square, is normalized to obtain a matrix whose values belongs to the set [0, 1] as follows

$$\bar{\Delta}(v, \varepsilon) = \frac{\Delta(v, \varepsilon) - \min_{v,\varepsilon} \Delta(v, \varepsilon)}{\max_{v,\varepsilon} [\Delta(v, \varepsilon) - \min_{v,\varepsilon} \Delta(v, \varepsilon)]}. \quad (65)$$

Then, the resulting matrix  $\bar{\Delta}(v, \varepsilon)$  is filtered with a bank of Gabor filters whose impulse responses are

$$\psi_{m,l}(x, y) = \frac{f_l^2}{\pi\gamma\eta} e^{-\left(\frac{f_l^2}{\gamma^2}x^2 + \frac{f_l^2}{\eta^2}y^2\right)} e^{j2\pi f_l x'} \quad (66)$$

with

$$\begin{aligned} x' &= x \cos(\theta_m) + y \sin(\theta_m) \quad \text{and} \\ y' &= -x \sin(\theta_m) + y \cos(\theta_m) \end{aligned} \quad (67)$$

for various  $f_l$  and  $\theta_m$ ,  $l = 0, \dots, L - 1$ ,  $m = 0, \dots, M - 1$ , where  $L$  and  $M$  are the numbers of selected spatial central frequencies and orientation angles, respectively. The choice of the  $f_l$  and  $\theta_m$  depends on the specific application and on the worst case image to represent with the moments. The selection of these parameters has to be conducted in order

to get an accurate representation of the image under test. In fact, since by varying  $\theta_m$ , the harmonic response of the filter moves on a circumference, whose radius is  $f_l$ , it is possible to extract local characteristics in the Fourier domain by choosing a set of values for the two parameters [21]. The value of each pixel of the output image is given by the convolution product of the Gabor function and the input image  $\bar{\Delta}(v, \varepsilon)$  as

$$\begin{aligned} g_{l,m}(v, \varepsilon; f_l, \theta_m) &= \psi_{l,m}(v, \varepsilon; f_l, \theta_m) * \bar{\Delta}(v, \varepsilon) \\ &= \int_{-\infty}^{\infty} \int_{-\infty}^{\infty} \psi_{l,m}(v - v_\tau, \varepsilon - \varepsilon_\tau; f_l, \theta_m) \bar{\Delta}(v_\tau, \varepsilon_\tau) dv_\tau d\varepsilon_\tau \end{aligned} \quad (68)$$

with  $l = 0, \dots, L - 1$  and  $m = 0, \dots, M - 1$ , where  $L$  and  $M$  are the numbers of central frequency and orientation angles, respectively. Finally, the outputs of the filters are processed to extract the feature vector used to classify the targets. In particular, a feature is extracted from the output image of each filter by adding up the values of all pixels [21], as

$$F_q = g_{l,m} = \sum_v \sum_\varepsilon |g_{l,m}(v, \varepsilon; f_l, \theta_m)| \quad (69)$$

where  $q = mL + l$ , with  $l = 0, \dots, L - 1$  and  $m = 0, \dots, M - 1$ ,  $N_v$  and  $N_\varepsilon$  are the dimensions of the image  $\bar{\Delta}$  along both axis.

## IV. PERFORMANCE ANALYSIS

In this section, the proposed model is tested with both simulated data and real data acquired from replicas of the targets of interest. The targets are divided in two classes, which are *warhead* and *confusing object*. Moreover, both of them are divided in subclasses, which are associated to a particular type of target. Specifically, the *warhead* class is composed by two subclasses: cone and cone with triangular fins at the base, which are replicas of warhead without and with fins, respectively. *Confusing object* class, in contrast, is divided in three subclasses: sphere, cone, and cylinder.

The conical warhead has a diameter  $d$  of 0.75 m and a height  $h$  of 1 m, while the fin's base  $b_f$  is 0.20 m and the height  $h_f$  is 0.50 m, as shown in Fig. 10(a). The sizes of the confusing objects are usually comparable with the dimensions of the warheads in order to confuse the antimissile radar system. Therefore, both the cylindrical and conical objects are chosen to have a diameter and a height equal to 0.75 and 1 m, respectively, while the sphere diameter is 1 m, as shown in Fig. 10(b).

In order to analyze the performance of the proposed algorithm, three figures of merit are considered, which are the *Probability of correct Classification* ( $P_C$ ), the *Probability of correct Recognition* ( $P_R$ ), and the *Probability of Unknown* ( $P_U$ ). The meaning of classification is the ability to distinguish between the warhead class and the confusing object class, while recognition means the capability to identify the actual shape of the target within the warhead and the confusing object class. Finally,  $P_U$  is computed as the ratio of the number of analyzed objects for which the

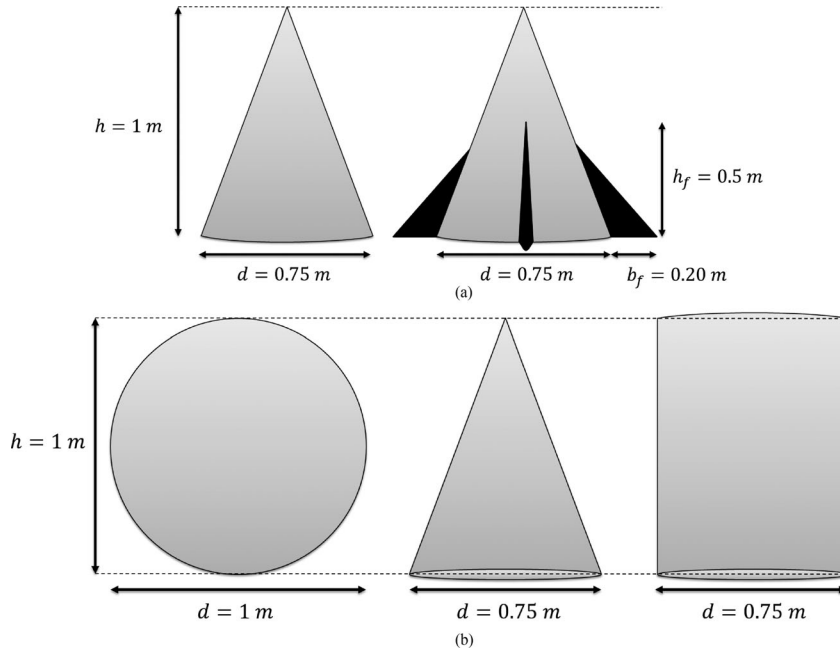


Fig. 10. Dimensions of the replicas of the targets of interest. (a) Warheads. (b) Confusing objects.

classifier does not make a decision and the total number of analyzed objects. A Monte Carlo approach is used in order to calculate the mean of the three figures of merit over several cases. Specifically, the means are evaluated over 50 different Monte Carlo runs in which all the available signals are divided randomly into training or testing sets with 70% used for training and 30% for testing. The  $k$  value of classifier has to be chosen greater than 1 in order to consider the *unknown* class; especially it is set to 3 for the ACVD and Gabor filter based methods, while it is 5 for the pZ based one. These two specific values of  $k$  are selected as they resulted to provide the best performance for the three approaches.

The performance is shown for varying the signal to noise power ratio (SNR) and observation time, which is either 10, 5, or 2 s. Moreover, for both the pZ and the Gabor filter methods, the dimension of the feature vector is also varied. The spectrogram is computed using a Hamming window with 75% overlap. The number of points for the DFT computation  $N_{\text{bin}}$  is fixed for the ACVD approach, whereas it is adaptively evaluated for the pZ and the Gabor filter methods, in order to obtain a square representation of the spectrogram. Specifically, in these cases  $N_{\text{bin}}$  is given by

$$N_{\text{bin}} = \left\lceil \frac{N - W \text{ overlap}}{W (1 - \text{overlap})} \right\rceil \quad (70)$$

where  $N$  is the number of signal samples,  $\lceil \cdot \rceil$  represents the smaller integer greater than or equal to the argument, and  $\text{overlap}$  is the percentage of overlap expressed in the interval  $[0, 1]$ . Finally, it is assumed that the effect of the principal translation motion of the targets is compensated before the signals are processed.

#### A. Simulated Data

The database for simulated data is composed of 105 realizations of the received signal for each target of interest, obtained by considering 15 signals for 7 different values of the elevation angle  $\alpha_E$  as follows:

$$\alpha_E = \varepsilon 15^\circ \quad \text{with} \quad \varepsilon = 0, \dots, 6 \quad (71)$$

while the azimuth angle  $\alpha_A$  is set to  $0^\circ$ . The initial phase of the micromotions is taken randomly in uniform distribution  $[0, 2\pi]$  and an additive white Gaussian noise is added to each simulation.

Fig. 11(a) shows  $P_C$  and  $P_R$  for the ACVD-based feature vector approach. It is clear that both of them increase as the SNR increases, while showing a slight difference as the signal's duration varies. Moreover,  $P_C$  and  $P_R$  become similar as the noise decreases. Observing Fig. 11(b), which shows  $P_U$ , it is noted that it is almost constant at about 0.1, for all the values of SNR and signal duration considered. Defining the probability of misclassification  $P_M$  as

$$P_M = 1 - P_C - P_U \quad (72)$$

and since  $P_C$  is slightly greater than 0.9 for SNR greater than 0 dB, it is clear that  $P_M$  decreases as the SNR increases, becoming smaller than  $10^{-2}$ .

Fig. 12 shows the performance obtained by using the pZ-based approach. In this case the dimension of the feature vector  $Q$  depends on the polynomial order which, in turn, determines the number of pZ moments. Observing Fig. 12(a), (b), (d), (e), (g), and (h), it is clear that the performance generally improves as the signal's duration and the moments order increases. Moreover, for SNR greater than 0 dB, the gap between  $P_C$  and  $P_R$  becomes negligible as the moments order increases, and both of them

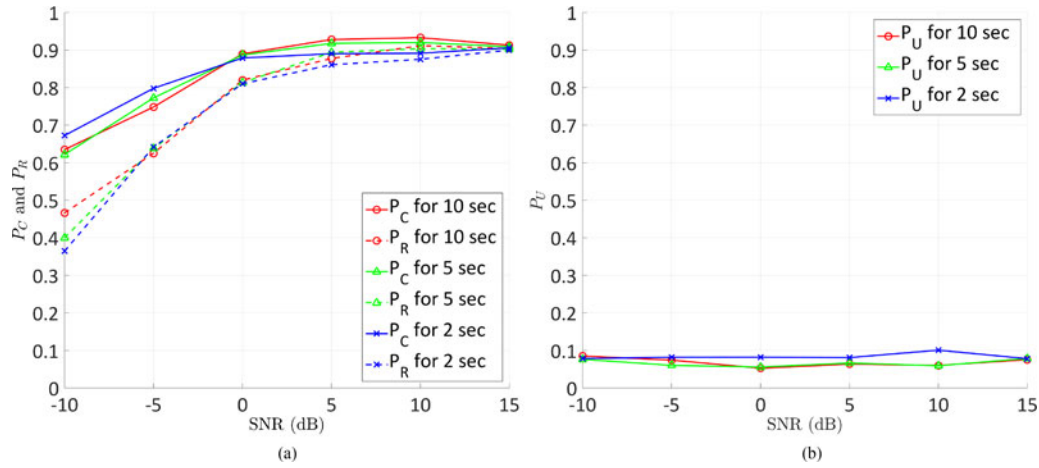


Fig. 11. Performance of the ACVD-based feature vector approach for simulated data on varying the signal's duration and the SNR. (a)  $P_C$  and  $P_R$ . (b)  $P_U$ .

reach probabilities of about 0.99 for order greater than 8. Fig. 12(c), (f), and (i) represent the performance in terms of  $P_U$ . It is possible to observe that, for SNR greater than  $-5$  dB, the performance generally improves as both signal duration and moments order increase. For observation times of 5 and 2 s,  $P_U$  is smaller than 0.1, for orders greater than 4 and for all the noise levels; in contrast, for duration equal to 10 s and for SNR of  $-10$  dB,  $P_U$  is about 0.1, while for lower noise levels  $P_U$  becomes smaller than  $10^{-2}$  as the order increases.

Fig. 13 shows  $P_C$ ,  $P_R$ , and  $P_U$  for the Gabor filter approach. For this approach, the dimension of feature vector corresponds to the number of filters, which depends on the orientation angular step  $\theta_{\text{step}}$ . Recall that the number of features,  $Q$  is given by

$$Q = L \left( \left\lceil \frac{\pi/2}{\theta_{\text{step}}} \right\rceil + 1 \right) \quad (73)$$

where  $\theta_{\text{step}}$  is the orientation angular step and  $L$  is the number of central frequencies. The latter was fixed at four values; 0.5, 1, 1.5, and 2. The value of  $\theta_{\text{step}}$  was set to be an integer in the interval  $[3^\circ, 10^\circ]$ . In this way, an analysis on varying the density of the considered positions of the harmonic response on each circumference with radius equal to  $f_l$  is conducted. The values of the orientation angle,  $\theta_m$ , is given by

$$\theta_m = m \theta_{\text{step}} \quad (74)$$

with  $m = 0, \dots, M - 1$  and where

$$M = \left\lceil \frac{\pi/2}{\theta_{\text{step}}} \right\rceil. \quad (75)$$

From (74) and (75), it is important outlining that the features are extracted moving the harmonic response of the filter considering only the first quadrant, due to the symmetry of the expected image for this application.

Fig. 13(a), (b), (d), (e), (g), and (h) show that  $P_C$  and  $P_R$  are approximately equal, and for a signal duration of 2 s, they increase quickly, becoming greater than 0.98 for

SNR greater than  $-5$  dB. For signal durations of 5 and 10 s, instead,  $P_C$  and  $P_R$  are greater than 0.98 for all the considered values of SNR and  $Q$ . As shown in Fig. 13(c), (f), and (i),  $P_U$  is always smaller than 0.05. Finally it is noted that the performance does not change significantly when varying the feature vector dimension.

## B. Real Data

Fig. 14 shows the experiment setup used to acquire the real data. The real data was acquired from signals scattered from targets of interest with a representative radar. Particularly, ten acquisitions of 10 s were made for each target and for each of the possible nine pair of azimuth and elevation angles formed using three values for both of them, namely  $[0^\circ; 45^\circ; 90^\circ]$ . The acquisition of 10 s has been also split into segments of 5 and 2 s for the analysis on the signal duration. The parameters of the micromotions were chosen as for simulated data, and the precession, nutation, and wobbling were simulated using an ST robotic manipulator R-17 and an added rotor [26], for both warheads and confusing objects. As it can be noted from pictures in Fig. 14, which shows the experiment setup, the robotic arm is wrapped with anechoic material such that acquired signals contain only the micro-Doppler from the targets. The rotor is attached to the wrist of the robotic arm and it is used to simulate the warhead spinning and confusing objects wobbling. Moreover, by means of a synchronized and perturbed rotation of robotic arm and the wrist, the conical movement and nutation are simulated. It has to be underlined that the trajectory of ballistic targets is not taken into account in the experiment considering that the principal movement of the object is compensated. In this way, the classification is based only on the micromotions of targets of interest.

Fig. 15 represents an example of spectrogram of a warhead with fins obtained by using both simulated and real data. It is possible to note that the two spectrograms show the same trend, where the precession leads to a modulation of the maximum Doppler, which is due to the fins rotation.

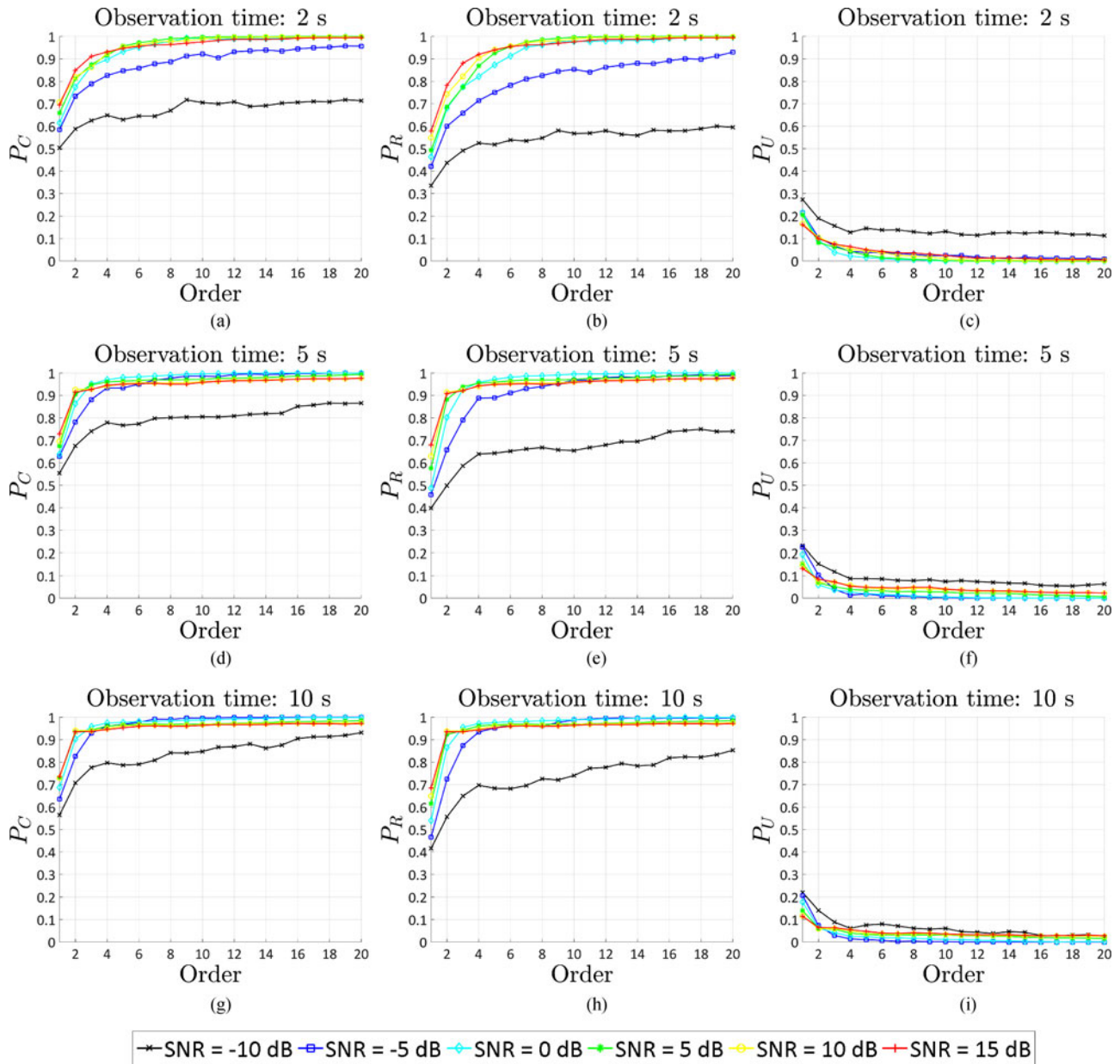


Fig. 12. Performance of the pZ-based feature vector approach for simulated data; the analysis is conducted on varying the order, the signal's duration, and the SNR. (a)  $P_C$ . (b)  $P_R$ . (c)  $P_U$ . (d)  $P_C$ . (e)  $P_R$ . (f)  $P_U$ . (g)  $P_C$ . (h)  $P_R$ . (i)  $P_U$ .

Moreover, it is pointed out that the main differences between the simulated and the real case are due to the fact that in the presented simulation model the RCS of the scatterers is not taken into account, and the initial phase of the micromotions is random in both two cases. The performance is evaluated by varying the signal duration and the SNR, as for the simulated data. In addition, assuming that the noise for the acquired signals in a controlled environment is negligible, the analysis on the SNR was conducted by adding white Gaussian noise to the real data. Finally before processing, the received signals are down-sampled by a factor of 10.

Fig. 16(a) shows  $P_C$  and  $P_R$ , while Fig. 16(b) shows the  $P_U$  for the ACVD-based method. The performance trend

obtained in the previous section for the simulated data is confirmed by the real data. In fact, both  $P_C$  and  $P_R$  increase as the SNR increases; however, the effect of changing the observation time is more evident in this case. Moreover, the gap between the two figures of merit decreases as both the duration of the signals time and the SNR increase. Observing Fig. 16(b),  $P_U$  is almost constant for all analyzed cases and it is smaller than 0.1.

Fig. 17 shows the results obtained by using the pZ-based approach. Fig. 17(a), (b), (d), (e), (g), and (h) show that, even on real data,  $P_C$  and  $P_R$  generally improves as the moments order and the SNR increase. However, they both decrease as the signal duration increases. In particular, this trend is more evident for low values of SNR. Moreover, ob-

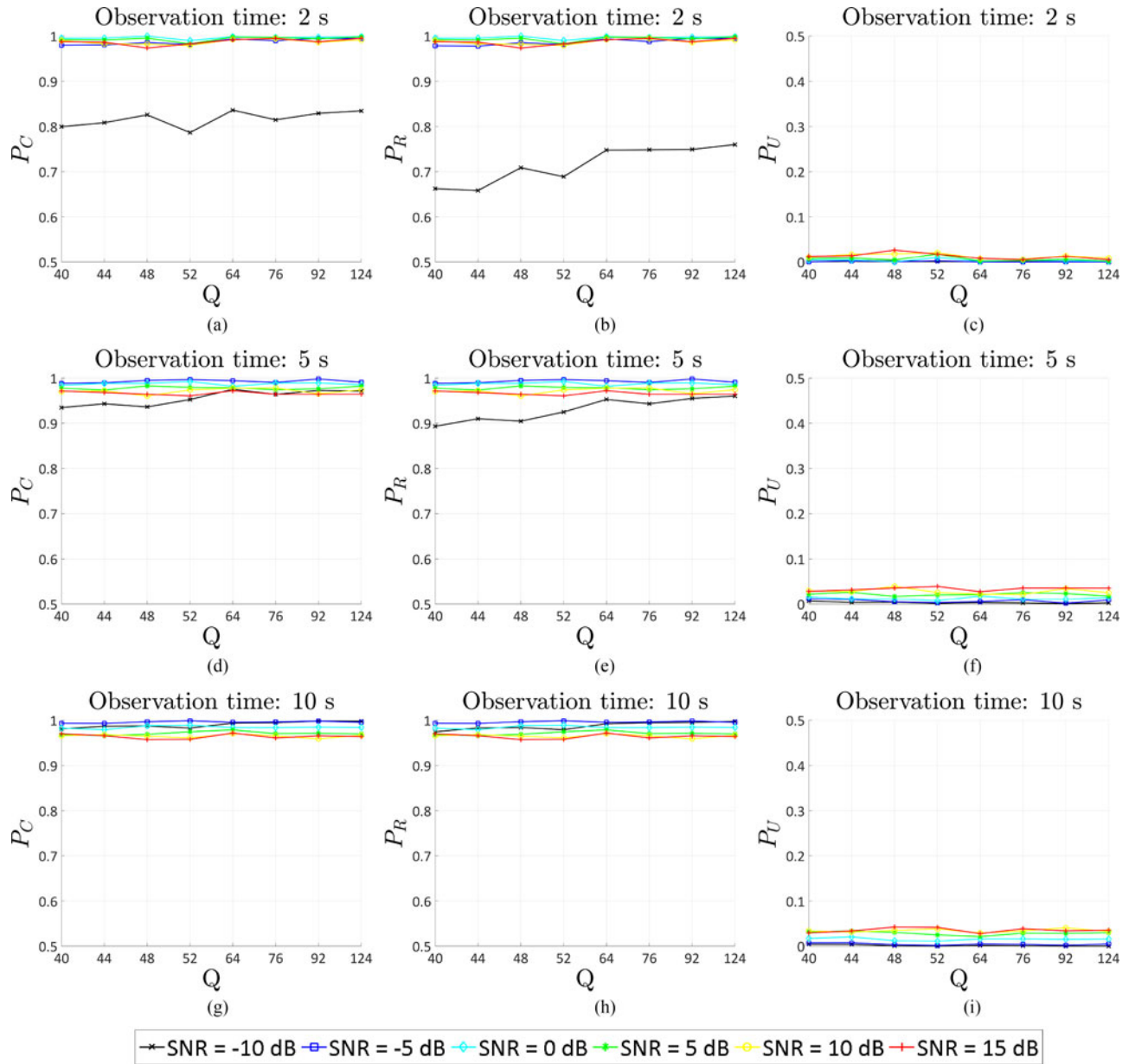


Fig. 13. Performance of the Gabor Filter based feature vector approach for simulated data; the analysis is conducted on varying the number of features  $Q$ , the signal's duration, and the SNR. (a)  $P_C$ . (b)  $P_R$ . (c)  $P_U$ . (d)  $P_C$ . (e)  $P_R$ . (f)  $P_U$ . (g)  $P_C$ . (h)  $P_R$ . (i)  $P_U$ .

servicing Fig. 17(c), (f), and (i), it is clear that  $P_U$  increases as the observation time increases. The reason of this behavior seems likely to be due to the choice of the k-means classifier. In fact, for greater values of the signal duration, the feature vectors of a given class occupy a smaller region in the multidimensional space: then, it is more likely that a feature vector under test is not close enough to be classified as belonging to the correct class. A different classifier, less dependent on distances in the multidimensional space might produce different results. Moreover,  $P_U$  decreases as the SNR and the moments order increases. The gap between  $P_C$  and  $P_R$  becomes smaller as the moments order increases. However, unlike the performance obtained

on simulated data, the maximum value reached by the two probabilities is around 0.90.

Fig. 18 shows the performance of the Gabor filter based method. Observing Fig. 18(a), (b), (d), (e), (g), and (h), it is clear that both  $P_C$  and  $P_R$  increase as the SNR and observation time increase. In particular, for signal duration of 5 s, both  $P_C$  and  $P_R$  are greater than 0.98 for SNR greater than  $-10$  dB; for duration equal to 10 s, instead,  $P_C$  is greater than 0.99 for the all analyzed cases. Finally, the gap between the two probabilities decreases as the SNR increases, and they tend to become equal for high values of the SNR. Fig 18(c), (f), and (i) show  $P_U$  versus  $Q$ , which is clearly smaller than 0.05 for all the analyzed case, from

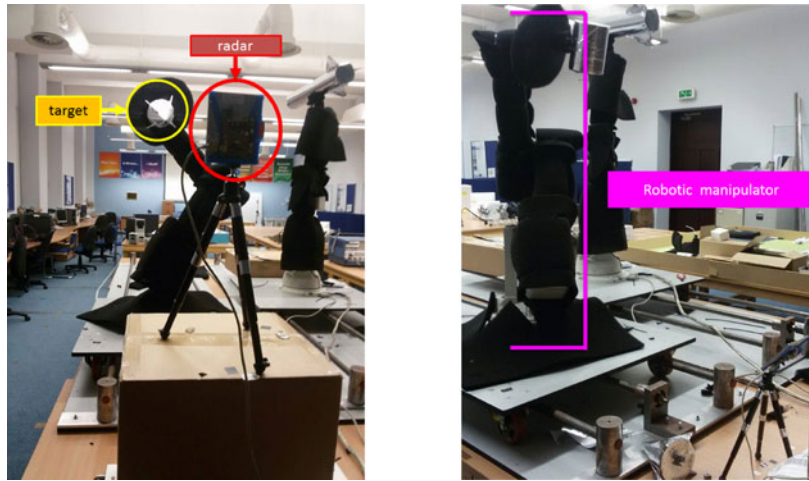


Fig. 14. Experiment setup.

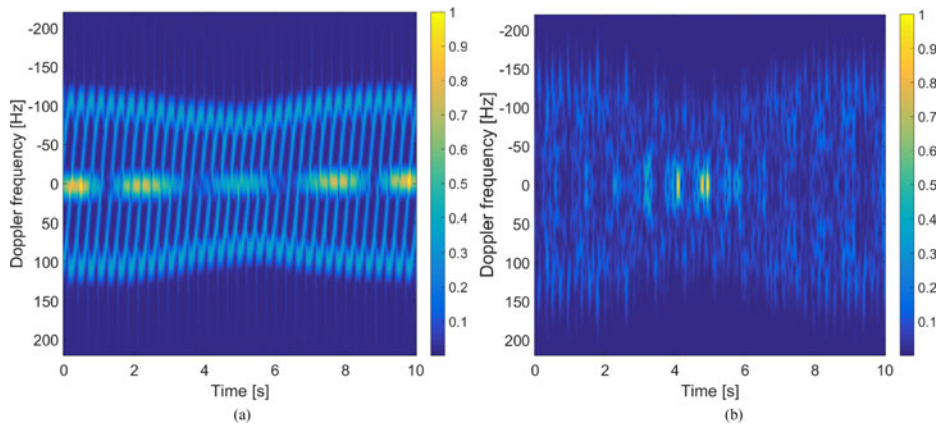


Fig. 15. Example of spectrogram obtained by a received signal from a warhead with fins. (a) Simulated data. (b) Real data.

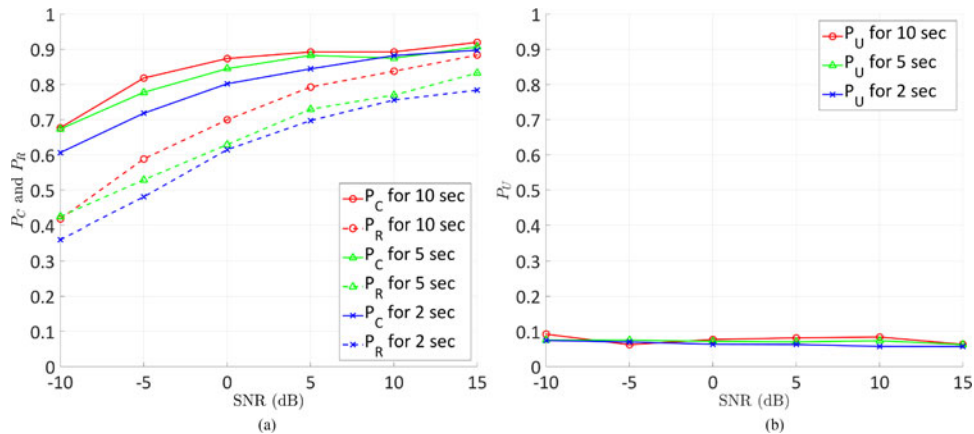


Fig. 16. Performance of the ACVD-based feature vector approach for real data on varying the signal duration and the SNR. (a)  $P_C$  and  $P_R$ . (b)  $P_U$ .

the results it is clear that higher is the SNR then higher are the performance.

### C. Performance in Presence of the Booster

The performance with real data was evaluated also in the case in which the received signal was scattered from an additional object different from warheads and confusing

objects. This analysis is of interest since, during the flight, the missile releases some debris in addition to the confusing objects, such as the booster used in the boost phase. As in the case of confusing objects, when the booster has been released by the missile, it starts to wobble, as shown in Fig. 19(a). However, the booster rotation velocity is smaller than the confusing objects', while its dimensions are bigger. In Fig. 19(b), the model used for the booster is shown. It

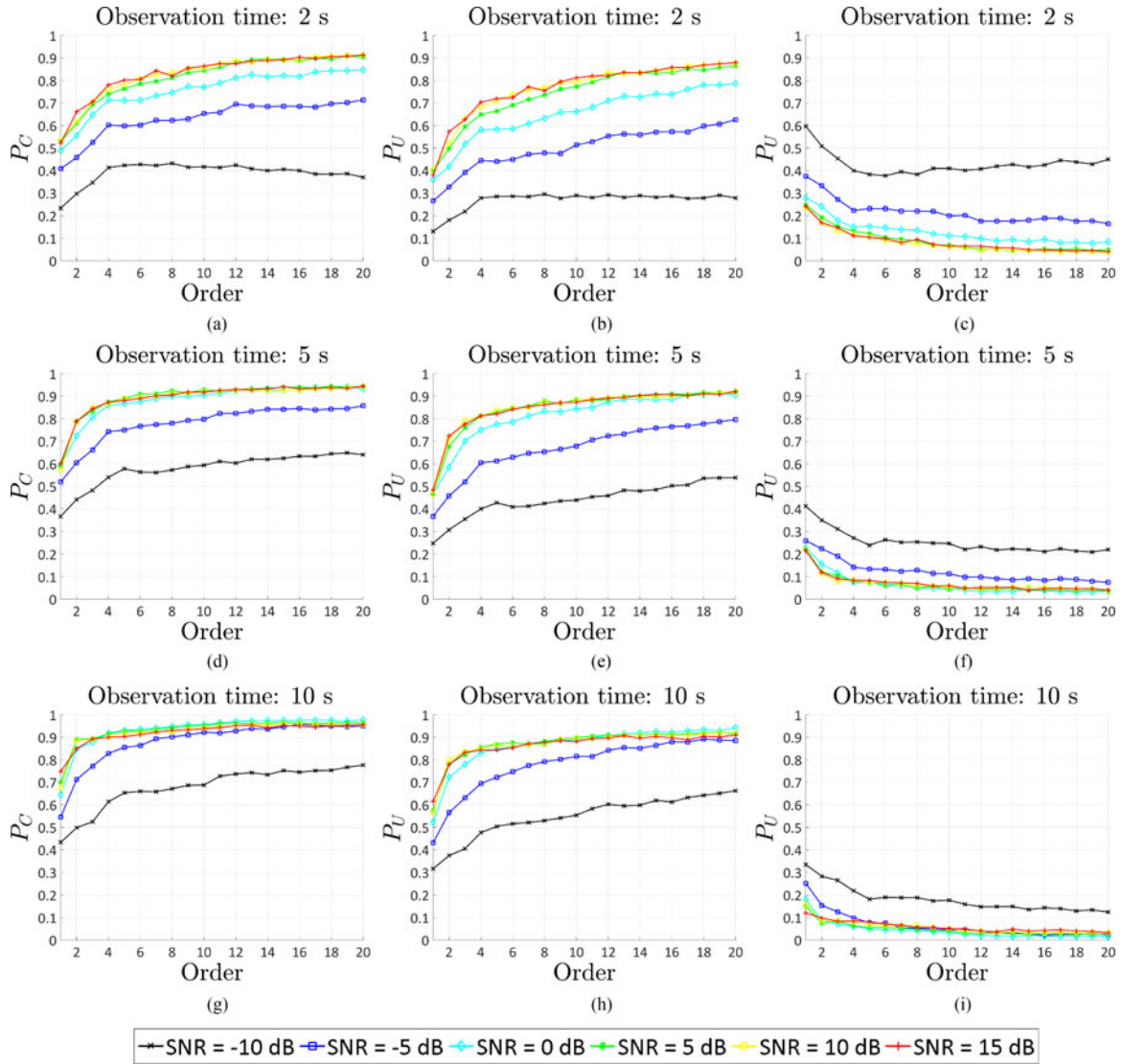


Fig. 17. Performance of the pZ-based feature vector approach for real data; the analysis is conducted on varying the moments order, the signal duration and the SNR. (a)  $P_C$ . (b)  $P_R$ . (c)  $P_U$ . (d)  $P_C$ . (e)  $P_R$ . (f)  $P_U$ . (g)  $P_C$ . (h)  $P_R$ . (i)  $P_U$ .

is assumed that the booster has a cylindrical shape, whose diameter and height are 0.75 and 5 m, respectively, with triangular fins, whose base is 0.50 m and height is 1 m; the wobbling velocity is one fifteenth of that of the confusing objects.

This analysis is conducted by training the classifier with feature vectors belonging to either warhead class or confusing object class, and then by testing it on the booster feature vector. Moreover, the performance is evaluated in terms of  $P_U$ , as defined above, and *probability of misclassification (Error) as a Warhead* ( $P_{eW}$ ), determined by the ratio of the number of times in which the booster is classified as a warhead and the total number of tests. Note, in this specific case, classifying the booster as unknown represents the correct classification as there is no specific *booster* class.

Fig. 20 shows  $P_U$  and  $P_{eW}$  obtained by the ACVD-based algorithm as the signal duration and the SNR are varied. From Fig. 20 it is observed that even if  $P_U$  increases and, consequently,  $P_{eW}$  decreases as the signal duration

increases,  $P_{eW}$  remains greater than  $P_U$ . Moreover, the performance does not change significantly on varying the SNR.

Results obtained by using the pZ-Based approach are shown in Fig. 21. Observing the figure it is clear that the probability of classifying the booster as unknown increases as the order grows up to 4, independently of the observation length, where the maximum value is reached, and it is above 0.80 for SNR equal to 0 and 5 dB. Considering orders greater than 4,  $P_U$  remains constant for positive values of SNR, while it significantly decreases for SNR smaller than 0 dB. However, for moments order of about 20,  $P_U$  grows as the SNR increases. It is noticed that  $P_{eW}$  decreases as the observation time increases for negative value of SNR, while it increases for SNR greater than 0 dB. However, the best results are obtained for positive values of the SNR and for signal duration of 2 and 5 s, reaching probabilities of error smaller than 0.20.

Finally,  $P_U$  and  $P_{eW}$  obtained for Gabor filter based feature vector are shown in Fig. 22. From the figure, one can



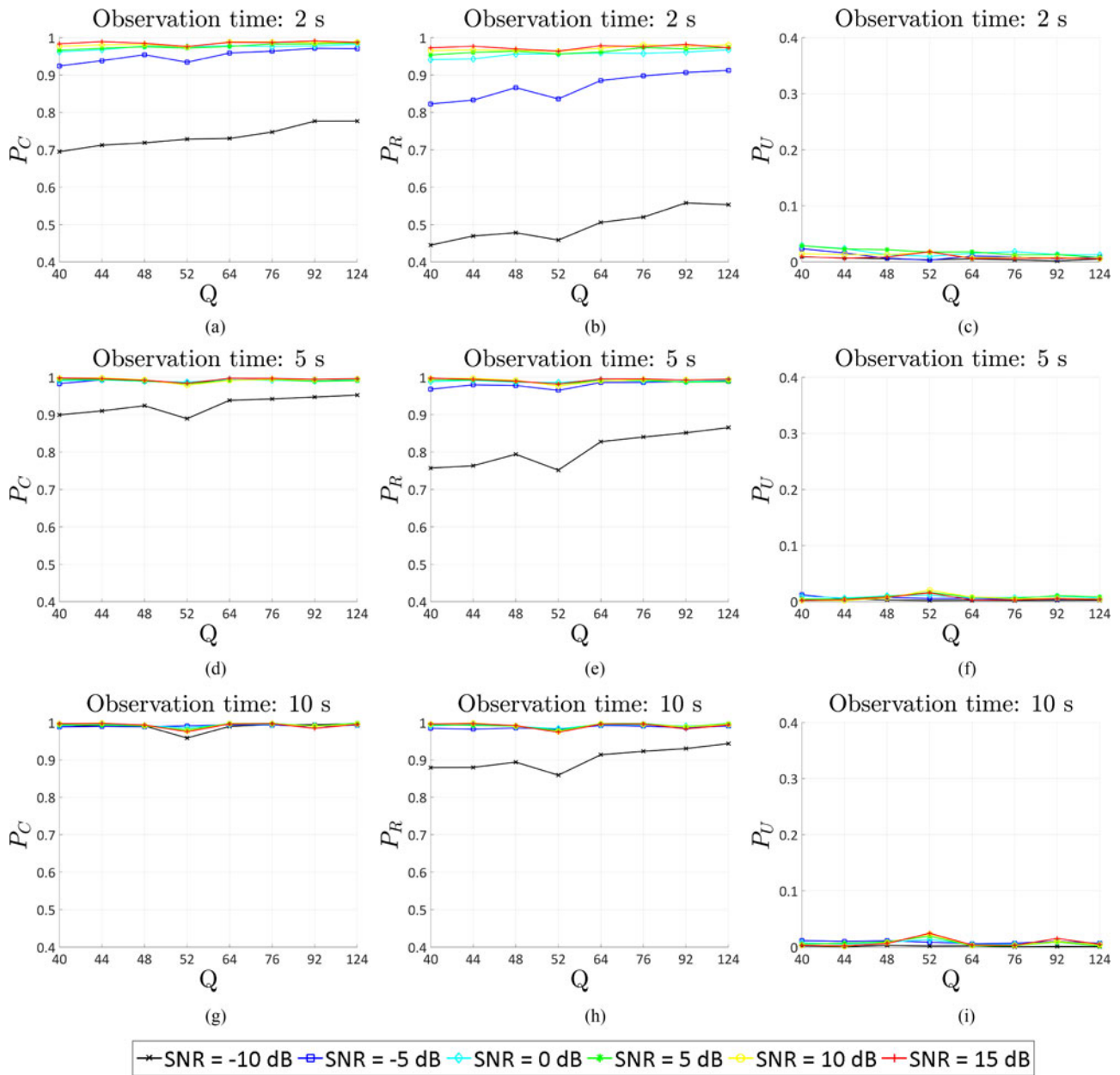


Fig. 18. Performance of the Gabor Filter based feature vector approach for real data; the analysis is conducted on varying the number of features  $Q$ , the signal duration and the SNR. (a)  $P_C$ . (b)  $P_R$ . (c)  $P_U$ . (d)  $P_C$ . (e)  $P_R$ . (f)  $P_U$ . (g)  $P_C$ . (h)  $P_R$ . (i)  $P_U$ .

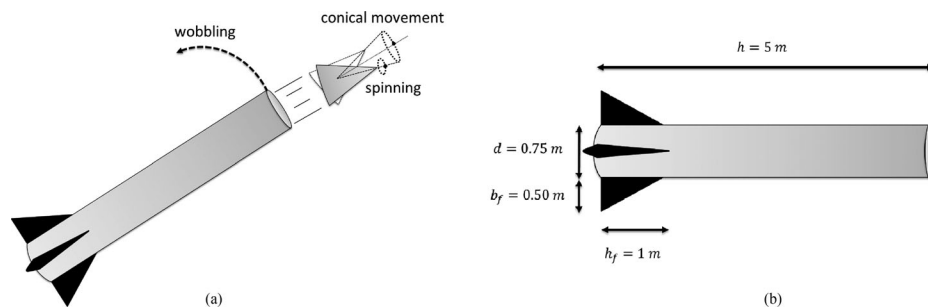


Fig. 19. Representation of Booster. (a) Difference of movement respect with warhead. (b) Dimensions model.

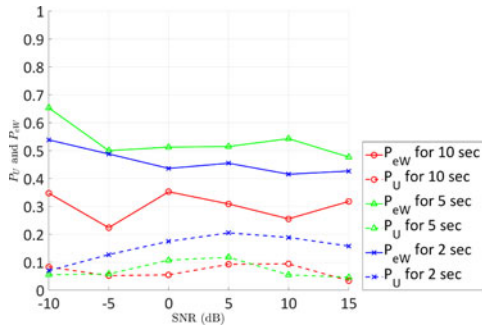


Fig. 20. Performance of the ACVD-based feature vector approach for real unknown data (booster); the analysis is conducted on varying the number of features  $Q$ , the signal duration and the SNR.

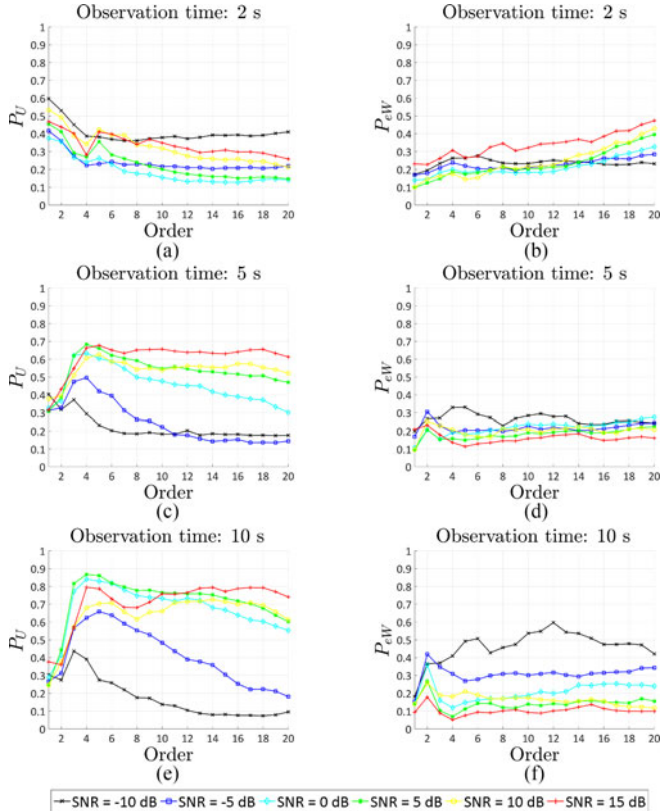


Fig. 21. Performance of the pZ-based feature vector approach for real unknown data (booster); the analysis is conducted on varying the moments order, the signal duration and the SNR. (a)  $P_U$ . (b)  $P_{eW}$ . (c)  $P_U$ . (d)  $P_{eW}$ . (e)  $P_U$ . (f)  $P_{eW}$ .

deduce that the performance improves as the signal duration and the SNR increase. In particular, the performance for the signal duration of 2 s is not useful because  $P_{eW}$  is always greater than  $P_U$ . However, for observation time of 5 s  $P_U$  becomes greater than  $P_{eW}$  from SNR greater than  $-10$  dB reaching about 0.90 for highest values of SNR. Finally, for signal duration equal to 10 s,  $P_U$  is constantly greater than 0.90 independently of the values of the SNR and  $Q$ ; on the other hand,  $P_{eW}$  is smaller than  $10^{-2}$  for values of the SNR greater than 0 dB.

Consequently it is clear that in the case of classification of unknown objects which are not used to train the classifier, such as the booster, the ACVD-based approach

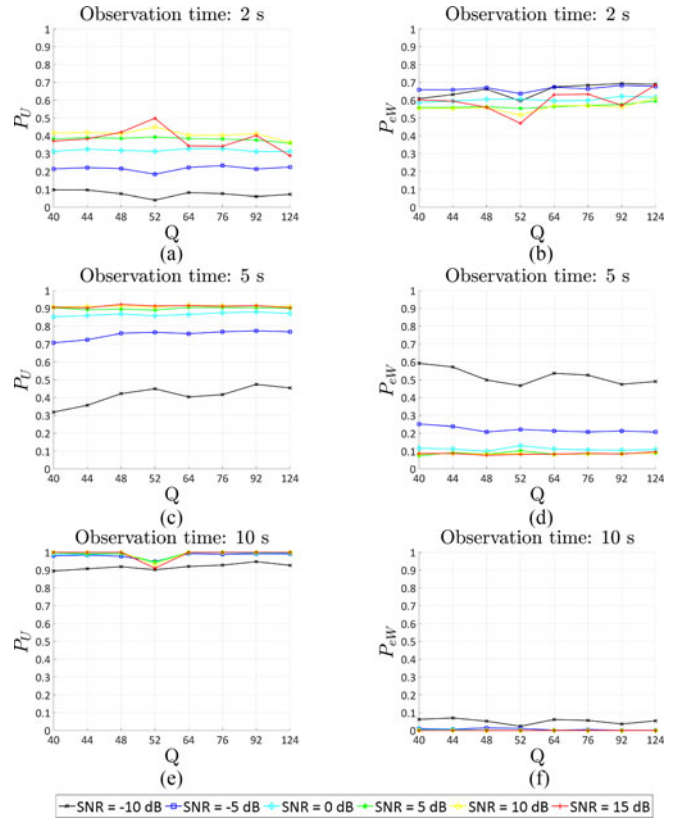


Fig. 22. Performance of the Gabor Filter based feature vector approach for real unknown data (booster); the analysis is conducted on varying the number of features  $Q$ , the signal duration and the SNR. (a)  $P_U$ . (b)  $P_{eW}$ . (c)  $P_U$ . (d)  $P_{eW}$ . (e)  $P_U$ . (f)  $P_{eW}$ .

does not guarantee satisfactory performance. The pZ-based approach is able to give good performance for small signal duration and for high SNR. Alternatively the Gabor filter approach provided the optimum results for an observation time of 5 s, for SNR greater than  $-10$  dB, and of 10 s, independently of the noise levels.

## CONCLUSION

In this paper, the capability of micro-Doppler-based recognition in the specific challenge of distinguishing between warheads and confusing objects has been evaluated. A high frequency based model of a received radar signal for the targets of interest has been presented, considering different scattering points and their occlusion effects on time. This signal model has been used to simulate the received signal from the targets on varying the elevation angle. By using a CW radar, instead, a real database has been obtained by acquiring signals scattered by replicas of the targets of interest on varying both the elevation and the azimuth angles. Subsequently, a framework comprising three different techniques for radar micro-Doppler classification based on the CVD have been presented. The reliability of these techniques has been demonstrated by testing them both on simulated and real micro-Doppler data. The results have shown that, for both the two cases, all the three approaches generally ensure a sufficient degree of correct classification. Finally, an analysis on real unknown data has

been conducted in order to test the presented methods also in the case in which the feature vector under test does not belong to one of the classes of interest, such as the booster separated from warhead. Even in this case the results have shown that for a sufficient observation time, the framework is able to recognize the unknown target. Future work will involve a study of the best micro-Doppler features for ballistic target classification in terms of computational cost and reliability. A new model based classification algorithm will be investigated that uses the proposed mathematical model in this paper.

## ACKNOWLEDGMENT

The data which underpin this paper is subject to a confidentiality agreement with one of the collaborators—as such the data cannot be made openly available. Enquiries about this restriction can be submitted to researchdataproject@strath.ac.uk in the first instance.

## REFERENCES

- [1] G. L. Silberman  
Parametric classification techniques for theater ballistic missile defense  
*In Proc. Johns Hopkins Apl. Tech. Dig.*, 1998, vol. 19, no. 3, pp. 323–339.
- [2] G. Hongwei, X. Liangui, W. Shuliang, and K. Yong  
Micro-Doppler signature extraction from ballistic target with micro-motions  
*IEEE Trans. Aerosp. Electron. Syst.*, vol. 46, no. 4, pp. 1969–1982, Oct. 2010.
- [3] L. Liu, D. McLernon, M. Ghogho, W. Hu, and J. Huang  
Ballistic missile detection via micro-Doppler frequency estimation from radar return  
*Digit. Signal Process.*, vol. 22, no. 1, pp. 87–95, 2012.
- [4] V. Chen, F. Li, S. Ho, and H. Wechsler  
Micro-Doppler effect in radar: Phenomenon, model, and simulation study  
*IEEE Trans. Aerosp. Electron. Syst.*, vol. 42, no. 1, pp. 2–21, Jan. 2006.
- [5] C. Clemente, L. Pallotta, I. Proudler, A. De Maio, J. Soraghan, and A. Farina  
Pseudo-Zernike-based multi-pass automatic target recognition from multi-channel synthetic aperture radar  
*IET Radar, Sonar Navig.*, vol. 9, no. 4, pp. 457–466, 2015.
- [6] F. Fioranelli, M. Ritchie, and H. Griffiths  
Multistatic human micro-Doppler classification of armed/unarmed personnel  
*IET Radar, Sonar Navig.*, vol. 9, no. 7, pp. 857–865, 2015.
- [7] L. Du, B. Wang, Y. Li, and H. Liu  
Robust classification scheme for airplane targets with low resolution radar based on EMD-clean feature extraction method  
*IEEE Sensors J.*, vol. 13, no. 12, pp. 4648–4662, Dec. 2013.
- [8] F. Fioranelli, M. Ritchie, and H. Griffiths  
Analysis of polarimetric multistatic human micro-Doppler classification of armed/unarmed personnel  
*In Proc. IEEE Radar Conf.*, May 2015, pp. 0432–0437.
- [9] S. Bjorklund, H. Petersson, A. Nezirovic, M. Guldogan, and F. Gustafsson  
Millimeter-wave radar micro-Doppler signatures of human motion  
*In Proc. 2011 Int. Radar Symp.*, Sep. 2011, pp. 167–174.
- [10] F. Fioranelli, M. Ritchie, and H. Griffiths  
Classification of unarmed/armed personnel using the netRAD multistatic radar for micro-Doppler and singular value decomposition features  
*IEEE Geosci. Remote Sens. Lett.*, vol. 12, no. 9, pp. 1933–1937, Sep. 2015.
- [11] P. Molchanov, K. Egiazarian, J. Astola, A. Totsky, S. Leshchenko, and M. Jarabo-Amores  
Classification of aircraft using micro-Doppler bicoherence-based features  
*IEEE Trans. Aerosp. Electron. Syst.*, vol. 50, no. 2, pp. 1455–1467, Apr. 2014.
- [12] C. Hornsteiner and J. Detlefsen  
Extraction of features related to human gait using a continuous-wave radar  
*In Proc. 2008 German Microw. Conf.*, Mar. 2008, pp. 1–3.
- [13] L. Liu, M. Popescu, M. Skubic, M. Rantz, T. Yardibi, and P. Cud-dihy  
Automatic fall detection based on Doppler radar motion signature  
*In Proc. 2011 5th Int. Conf. Pervasive Comput. Technol. Health-care*, May 2011, pp. 222–225.
- [14] I. Bilik, J. Tabrikian, and A. Cohen  
Target classification using Gaussian mixture model for ground surveillance Doppler radar  
*In Proc. 2005 IEEE Int. Radar Conf.*, May 2005, pp. 910–915.
- [15] A. Ghaleb, L. Vignaud, and J. Nicolas  
Micro-Doppler analysis of wheels and pedestrians in ISAR imaging  
*IET Signal Process.*, vol. 2, no. 3, pp. 301–311, Sep. 2008.
- [16] S. Bjorklund, T. Johansson, and H. Petersson  
Evaluation of a micro-Doppler classification method on MM-wave data  
*In Proc. 2012 IEEE Radar Conf.*, May 2012, pp. 0934–0939.
- [17] C. Clemente, A. Balleri, K. Woodbridge, and J. Soraghan  
Developments in target micro-Doppler signatures analysis: Radar imaging, ultrasound and through-the-wall radar  
*EURASIP J. Adv. Signal Process.*, vol. 2013, no. 1, pp. 47–64, 2013.
- [18] C. Clemente, L. Pallotta, A. De Maio, J. Soraghan, and A. Farina  
A novel algorithm for radar classification based on Doppler characteristics exploiting orthogonal pseudo-Zernike polynomials  
*IEEE Trans. Aerosp. Electron. Syst.*, vol. 51, no. 1, pp. 417–430, Jan. 2015.
- [19] A. Bhatia and E. Wolf  
On the circle polynomials of Zernike and related orthogonal sets  
*In Math. Proc. Cambridge Philosoph. Soc.*, 1954, vol. 50, no. 1, pp. 40–48.
- [20] M. R. Teague  
Image analysis via the general theory of moments\*  
*J. Opt. Soc. Amer.*, vol. 70, no. 8, pp. 920–930, Aug. 1980.
- [21] A. R. Persico, C. Clemente, C. V. Ilioudis, D. Gaglione, J. Cao, and J. Soraghan  
Micro-Doppler based recognition of ballistic targets using 2-d Gabor filters  
*In Proc. Sensor Signal Process. Defence Conf.*, Sep. 2015, pp. 1–5.
- [22] J.-K. Kamarainen, V. Kyrki, and H. Kalviainen  
Invariance properties of Gabor filter-based features—overview and applications  
*IEEE Trans. Image Process.*, vol. 15, no. 5, pp. 1088–1099, May 2006.
- [23] N. Mittal, D. Mital, and K. L. Chan  
Features for texture segmentation using Gabor filters  
*In Proc. 1999 7th Int. Conf. Image Process. Appl.*, Jul. 1999, vol. 1, pp. 353–357.
- [24] J. Ilonen, J.-K. Kamarainen, and H. Kalviainen  
Fast extraction of multi-resolution Gabor features  
*In Proc. 2007 14th Int. Conf. Image Anal. Process.*, Sep. 2007, pp. 481–486.

[25] R. M. Murray, Z. Li, S. Sastry, and S. Sastry  
*A Mathematical Introduction to Robotic Manipulation*. Boca  
Raton, FL, USA: CRC press, 1994.

[26] S. A. P. Ltd. Maharashtra, India, Robotics within reach  
Tech. Rep. [Online]. Available: [http://www.strobots.com/  
images/Brochure.pdf](http://www.strobots.com/images/Brochure.pdf)

**Adriano Rosario Persico** (S'15) was born in Napoli, Italy, on October 7, 1988. He received the B.Sc. and M.Sc. degrees from Università degli Studi di Napoli Federico II, Naples, Italy, in 2011 and 2014, respectively, in telecommunications engineering. He is currently working toward the Ph.D. degree at the Centre for Signal and Image Processing, University of Strathclyde, Glasgow, U.K., under the supervision of Prof. J. Soraghan and Dr. C. Clemente.

Focus of his Ph.D. research is on new advanced signal processing methods and algorithms for space situation awareness and defense against airborne threats. His current research interests include radar micro-Doppler, compressed sensing, MIMO system and space-based radar design for multi-target detection, localization, and recognition for space situation awareness.

**Carmine Clemente** (S'09–M'13) received the Laurea cum laude (B.Sc.) and Laurea Specialistica cum laude (M.Sc.) degrees in telecommunications engineering from Università degli Studi del Sannio, Benevento, Italy, in 2006 and 2009, respectively. He received the Ph.D. degree from the Department of Electronic and Electrical Engineering, University of Strathclyde, Glasgow, U.K., in 2012.

Currently, he is a Lecturer in the Department of Electronic and Electrical Engineering, University of Strathclyde, Glasgow, U.K. working on advanced Radar signal processing algorithm, MIMO radar systems, and micro-Doppler analysis. His research interests include synthetic aperture radar focusing and bistatic SAR focusing algorithms development, micro-Doppler signature analysis and extraction from multistatic radar platforms, micro-Doppler classification, and statistical signal processing.

**Domenico Gaglione** (S'13) received the B.Sc. and M.Sc. degrees from Università degli Studi di Napoli Federico II, Naples, Italy, in 2011 and 2013, respectively, in telecommunications engineering. He is currently working toward the Ph.D. degree at the Centre for Signal and Image Processing, University of Strathclyde, Glasgow, U.K., under the supervision of Prof. J. Soraghan and Dr. C. Clemente.

He has been recently appointed as a Research Assistant for the work package 4 within the LSSCN consortium of the UDRC phase II initiative, whose focus is the development of novel paradigms for Distributed MIMO Radar Systems. His research interests include micro-Doppler-based and SAR-based classification and identification, compressive sensing based radar techniques, MIMO radar signal processing, and joint radar-communication system.

Mr. Domenico received the First Prize at the Student Paper Competition of the 2015 IEEE International Radar Conference, Arlington, VA, USA.

**Christos V. Ilioudis** (S'13) was born in Thessaloniki, Greece, on August 25, 1988. He received the Diploma degree from the Department of Informatics and Telecommunications Engineering, University Of Western Macedonia, Kozani, Greece, in 2012 and the M.Sc. degree with distinction in electronics and electrical engineering from the University of Strathclyde, Glasgow, U.K., in 2013. He has been working toward the Ph.D. degree at the Centre in Signal and Image Processing, Department of Electronic and Electrical Engineering, University of Strathclyde, since 2014 with research focus on waveform design for MIMO Radar system.

He recently became a Research Assistant on the UDRC phase II work package 4 within LSSC consortium, with research focused on the design of novel waveform libraries and paradigms specialized for Distributed MIMO Radar Systems.

His current research interests include MIMO radar systems, fractional waveform libraries, constant envelope fractional Fourier transform, radar waveform design, ambiguity function shaping, and orthogonal chirp division multiplexing.

Mr. Ilioudis received the third position in the best student paper competition at IEEE International Radar Conference 2015, Arlington, USA. Also his paper was within the ten best papers (finalists) in the same competition at IEEE International Radar Conference 2016, Philadelphia, PA, USA.

**Jianlin Cao** (S'13) received the B.Eng. (Hons) degree in electronic and electrical engineering from the University of Strathclyde, Glasgow, U.K., in 2013. He is currently working toward the Ph.D. degree at Centre in Signal and Image Processing, Department of Electronic and Electrical Engineering, University of Strathclyde, since 2013 with research focus on femtosatellite and synthetic aperture radar application.

After graduating, he joined the Centre for Signal and Image Processing and Advanced Space Concepts Laboratory in October 2013. He is a Visiting Research Student at the University of Glasgow, Glasgow, U.K. since October 2014.

**Luca Pallotta** (S'12–M'15) received the Laurea Specialistica degree (cum laude) in telecommunication engineering from the University of Sannio, Benevento, Italy, in 2009, and the Ph.D. degree in electronic and telecommunication engineering from the University of Naples Federico II, Naples, Italy, in 2014.

His research interests include the field of statistical signal processing, with emphasis on radar signal processing and radar targets classification.

Dr. Pallotta received the Student Paper Competition at the IEEE Radar Conference 2013.

**Antonio De Maio** (S'01–A'02–M'03–SM'07–F'13) was born in Sorrento, Italy, on June 20, 1974. He received the Dr.Eng. degree (with honors) and the Ph.D. degree in information engineering, both from the University of Naples Federico II, Naples, Italy, in 1998 and 2002, respectively.

From October to December 2004, he was a Visiting Researcher with the U.S. Air Force Research Laboratory, Rome, NY, USA. From November to December 2007, he was a Visiting Researcher with the Chinese University of Hong Kong, Hong Kong. Currently, he is a Professor with the University of Naples Federico II. His research interests include the field of statistical signal processing, with emphasis on radar detection, optimization theory applied to radar signal processing, and multiple-access communications.

Dr. De Maio received the 2010 IEEE Fred Nathanson Memorial Award as the young (less than 40 years of age) AESS Radar Engineer 2010 whose performance is particularly noteworthy as evidenced by contributions to the radar art over a period of several years, with the following citation for “robust CFAR detection, knowledge-based radar signal processing, and waveform design and diversity.”

**Ian Proudler** received the graduation degree in physics from Oxford University, Oxford, U.K., in 1978. He spent two years doing R&D work in the electronics industry before receiving the Ph.D. degree in digital signal processing from Cambridge University, Cambridge, U.K., in 1984.

He is currently a Professor of signal processing at Loughborough University, Loughborough, U.K. From 1986 until 2011, he was in the defense sector looking into various adaptive digital signal processing issues such as: numerical stability and efficient computation; antenna algorithm for HF communications; signal separation for ESM purposes; magnetic detection for maritime surveillance; and GPS antijam systems. He has published some 60 research papers, contributed to three textbooks and holds a patent on an adaptive filtering architecture.

Dr. Proudler received the John Benjamin Memorial Prize, in 1992 and 2001, and the IEE J. J. Thomson Medal, in 2002, for his work on signal processing algorithms. He was an Honorary Editor of *IEE Proceedings: Radar, Sonar and Navigation* for ten years. He has been on the organizing committee of several international conferences.

**John J. Soraghan** (S'83–M'84–SM'96) received the B.Eng. (Hons.) and M.Eng.Sc. degrees in electronic engineering from University College Dublin, Dublin, Ireland, in 1978 and 1983, respectively, and the Ph.D. degree in electronic engineering from the University of Southampton, Southampton, U.K., in 1989. His doctoral research focused on synthetic aperture radar processing on the distributed array processor.

After graduation, he was with the Electricity Supply Board in Ireland and with Westinghouse Electric Corporation in the USA. In 1986, he joined the Department of Electronic and Electrical Engineering, University of Strathclyde, Glasgow, U.K. as a Lecturer. He was a Manager of the Scottish Transputer Centre from 1988 to 1991, Manager with the DTI Parallel Signal Processing Centre from 1991 to 1995, and the Head of the ICSP from 2005 to 2007. He became a Professor of signal processing in 2003 and has held the Texas Instruments Chair in Signal Processing since 2004. He is currently the Director of the Sensor Signal Processing Research Groups within the Centre for Signal and Image Processing, University of Strathclyde, Glasgow, U.K. His main research interests include signal processing theories, algorithms, with applications to radar, sonar, and acoustics, biomedical signal and image processing, video analytics, and condition monitoring.

Prof. Soraghan has supervised 45 researchers to Ph.D. graduation and has published more than 340 technical publications. He is a Member of the IET.